they found multiple lesions in one section level, all suspected lesions were scored individually.

To evaluate the image sets, the basic image set (A) was used to detect a nonsolid hepatic lesion, which was observed as an area of low intensity on the T1-weighted image and as high and homogenous signal intensity, similar to that of fluid components, such as cerebrospinal fluid, on fat-saturated T2-weighted TSE images. After exclusion of nonsolid hepatic lesions, hepatic metastases were defined as solid nodules showing higher signal intensity than hepatic parenchyma on precontrast T2-weighted images in image set (A), diffusion-weighted images in (B), or postcontrast T2 or T2*-weighted images in (C) to (E). These criteria were presented as a reference to the evaluators, and the final decision was at the discretion of each reader.

Statistical Analysis

Based on the reviews of the 3 observers, an alternative free-response receiver operating characteristic (ROC) analysis was performed to evaluate the detection of all hepatic lesions. For each image set, an alternative free-response ROC curve was fitted to each evaluator's confidence rating using a maximum likelihood estimation program (ROCKIT 1.0.1 B2; Metz CE, University of Chicago, IL, 1998). The diagnostic accuracy of each image set for each observer and the composite data were calculated by measuring the area under the alternative free-response ROC curve (A_z). The relative sensitivity of detection was calculated for lesions allocated a rating of 4 or 5. The differences between image sets in terms of the mean A_z were analyzed with Bonferroni method for post hoc analysis when the overall differences determined by the repeated-measures analysis of variance were assessed considering a normal distribution. The sensitivity for the detection of hepatic metastases (on a per-lesion basis) and the positive predictive value for each image set were also calculated. Size-wise analyses of the lesions were conducted for all sizes of lesions, those larger than 1 cm, and those 1cm or smaller.[8] Lesions were categorized by size based on the final reference (ie, histopathologic findings, intraoperative ultrasonography, or preoperative images if an operation was not conducted). This was followed by a statistical comparison of sensitivity by means of the McNemar test.

To assess interobserver variability in interpreting images, κ statistics were calculated to measure the degree of agreement; κ values of 0.00 implied poor agreement; 0.01 to 0.20, slight agreement; 0.21 to 0.40, fair agreement; 0.41 to 0.60, moderate agreement; 0.61 to 0.80, substantial agreement; and 0.81 to 1.0, almost perfect agreement. A P value less than 0.05 was considered to indicate a statistically significant difference. All statistical analyses were performed using SPSS statistical software (SPSS version 15.0, SPSS Inc., Chicago, IL).

RESULTS

All MR examinations were completed successfully without any adverse effects.

Hepatic Lesions

There were 72 nonsolid lesions (54 cysts and 18 hemangiomas). Fifty-one nonsolid (36 cysts and 15 hemangiomas) lesions were diagnosed based on the characteristic findings of contrast-enhanced CT, gadolinium-enhanced MR imaging, or ultrasonography, and the other 21 lesions (18 cysts and 3 hemangiomas) were pathologically confirmed at resection. Of the 82 eligible patients, after exclusion of these nonsolid lesions, 38 patients had a total of 111 focal hepatic metastatic lesions, and 44 patients had no focal hepatic lesions in the total of 82 patients. Of the 111 metastatic lesions, 45 hepatic metastatic lesions (28 lesions larger than 1 cm, 17 lesions 1 cm or smaller) in 20 patients were pathologically confirmed by surgical resections or biopsies. The remaining 57 hepatic lesions (29 lesions larger than 1 cm, 28 lesions 1 cm or smaller) in 11 patients were nonpathologically diagnosed based on the interval growth on follow-up images and on clinical courses. Nine lesions in 7 patients were excluded because of the following reasons: 2 lesions (both smaller than 1 cm) in 2 patients could not be pathologically confirmed using the excised specimen; 7 lesions (3 lesions larger than 1 cm, 4 lesions 1 cm or smaller) in 5 patients proved difficult to diagnose based on interval evaluation or clinical courses. Therefore, a total of 102 focal hepatic metastatic lesions in 31 patients were evaluated. Fifty-seven lesions were larger than 1 cm, and 45 lesions were 1 cm or smaller (mean size, 1.6 cm; range, 0.3–3.3 cm). The maximum number of malignant lesions in any patient was 7.

Interobserver Variability

The κ values for the 3 evaluators are summarized in Table 2. The analysis of interobserver agreement for all lesion groups and modalities indicated moderate to almost perfect agreements, and was very high in image set (E). Thus, the mean values were used for the analysis of accuracy (A_z) and pooled values were used for sensitivity and positive predictive values.

Accuracy

The mean A_z values obtained for the evaluation of hepatic lesions are presented in Table 3. The A_z values for image sets (B) to (E) were significantly greater than those for the basic image set (A) ($P < 0.001$). For the other MR image sets, (C) had the smallest values ($P < 0.001$) and (E) had the largest values, which were significantly larger than the others sets, including (B), ie, diffusion weighted imaging, irrespective of lesion size ($P < 0.001$). The nonenhanced image set (B) had similar values to those of (D) (n.s.).

Sensitivity

The pooled results for the sensitivity of detection of hepatic lesions for all 3 observers are summarized in Table 4. In the

TABLE 2. Level of Interobserver Agreement for the Detection of Hepatic Lesions

Lesion Sizes and Image Sets	Observers		
	1 vs. 2	2 vs. 3	1 vs. 3
All lesions			
A	0.65 ± 0.06	0.67 ± 0.07	0.64 ± 0.07
B	0.70 ± 0.06	0.71 ± 0.07	0.67 ± 0.06
C	0.68 ± 0.06	0.65 ± 0.07	0.70 ± 0.06
D	0.79 ± 0.05	0.75 ± 0.06	0.76 ± 0.05
E	0.82 ± 0.04	0.78 ± 0.05	0.81 ± 0.05
Lesions >1 cm			
A	0.68 ± 0.06	0.64 ± 0.07	0.65 ± 0.07
B	0.75 ± 0.05	0.76 ± 0.07	0.71 ± 0.05
C	0.71 ± 0.06	0.70 ± 0.07	0.73 ± 0.06
D	0.82 ± 0.05	0.78 ± 0.06	0.82 ± 0.05
E	0.85 ± 0.04	0.83 ± 0.05	0.83 ± 0.05
Lesions ≤1 cm			
A	0.63 ± 0.07	0.70 ± 0.07	0.62 ± 0.08
B	0.62 ± 0.06	0.65 ± 0.08	0.63 ± 0.08
C	0.64 ± 0.06	0.62 ± 0.07	0.65 ± 0.05
D	0.73 ± 0.05	0.70 ± 0.07	0.68 ± 0.06
E	0.77 ± 0.05	0.73 ± 0.05	0.79 ± 0.04

See Table 1 for a description of the image sets. Data are κ values ± standard errors of the mean. The total sample size was 102 lesions (lesions >1 cm were, n = 57; ≤1 cm, n = 45) in 31 patients.

TABLE 3. Areas Under the Receiver Operating Characteristic Curves (A_z Values) for the Detection of Hepatic Lesions

	Lesion Size		
Image Sets	**All (n = 102)**	**>1 cm (n = 57)**	**≤1 cm (n = 45)**
A	0.58 ± 0.05	0.62 ± 0.05	0.53 ± 0.05
B	0.81 ± 0.04*†	0.86 ± 0.04*†	0.76 ± 0.05*†
C	0.70 ± 0.05*	0.76 ± 0.06*	0.61 ± 0.05*
D	0.80 ± 0.04*†	0.84 ± 0.04*†	0.73 ± 0.05*†
E	0.90 ± 0.03*‡†§	0.93 ± 0.03*‡†§	0.87 ± 0.03*‡†§

See Table 1 for a description of the image sets. Data are mean Az values ± standard errors of the mean.

Significantly higher ($P < 0.05$) than image sets *A, ‡B, †C, and §D.

TABLE 4. Sensitivity for the Detection of Hepatic Lesions

Lesion Sizes and Image Sets	Sensitivity	95% CI	*P*
All lesions			
A	0.47 (145/306)	42, 53	
B	0.69 (211/306)	63, 74	*†
C	0.56 (172/306)	50, 62	*
D	0.66 (201/306)	60, 71	*†
E	0.77 (235/306)	72, 81	*†‡§
Lesions >1 cm			
A	0.51 (88/171)	44, 59	
B	0.73 (125/171)	66, 80	*†
C	0.60 (103/171)	52, 68	
D	0.71 (122/171)	64, 78	*†
E	0.81 (139/171)	75, 87	*†
Lesions ≤1 cm			
A	0.42 (57/135)	34, 51	
B	0.64 (86/135)	55, 72	*†
C	0.51 (69/135)	42, 60	
D	0.59 (79/135)	50, 67	*
E	0.71 (96/135)	63, 79	*†§

See Table 1 for a description of image sets. The total sample size was 102 lesions (lesions >1 cm, n = 57; ≤1 cm, n = 45) in 31 patients. Data are percentages. Data in parentheses were those used to calculate the sensitivity values. *P* values were calculated with the McNemar test.

Significantly higher ($P < 0.05$) than image sets *A, ‡B, †C, and §D.

CI indicates confidence interval.

all-lesion group, the sensitivity of image sets (B) to (E) was higher than that of the basic image set (A). Image set (E) had the highest sensitivity and was significant higher than the other image sets, including (B) ($P < 0.01$). Image sets (B) and (D) had comparable values (n.s.), which were significantly higher than those for (C) ($P < 0.01$). When classified by lesion size, similar patterns were observed, but some of the comparisons did not reach statistical significance, including the differences between (B) and (E) (Table 4).

Positive Predictive Value

The pooled positive predictive values for the detection of hepatic lesions are shown in Table 5. Irrespective of the lesion groups, the mean positive predictive values for the basic image set (A) were the lowest, followed by image set (C); those for image set (E) were the highest. The mean positive predictive values for image set (B) were lower than those for image set (D) for all lesions and for

TABLE 5. Positive Predictive Values for the Detection of Hepatic Lesions

Lesion Sizes and Image Sets	Positive Predictive Value	95% CI
All lesions		
A	0.76 (145/190)	70, 82
B	0.85 (211/247)	80, 90
C	0.81 (172/212)	75, 86
D	0.89 (201/226)	84, 93
E	0.94 (235/251)	90, 96
Lesions >1 cm		
A	0.81 (88/108)	73, 88
B	0.93 (125/134)	88, 97
C	0.85 (103/121)	78, 91
D	0.92 (122/132)	87, 96
E	0.95 (139/146)	90, 88
Lesions ≤1 cm		
A	0.70 (57/82)	58, 79
B	0.76 (86/113)	67, 84
C	0.76 (69/91)	66, 84
D	0.84 (79/94)	75, 91
E	0.91 (96/105)	84, 96

See Table 1 for a description of the image sets. The total sample size was 102 lesions (lesions >1 cm, n = 57; ≤1 cm, n = 45) in 31 patients. Data are percentages. Data in parentheses were those used to calculate the positive predictive values.

CI indicates confidence interval.

lesions 1 cm or smaller, whereas those for image set (B) were slightly higher than those for image set (D) for lesions larger than 1 cm.

The majority of false-positive lesions were blurring and motion artifacts such as physical movement, respiratory motion (Fig. 1) and cardiovascular pulsation (Fig. 2), benign lesions (ie, bile duct adenoma, biliary hamartoma, hemangioma), and partial volume effect of hepatic tissue. MR image set (B) had relative lower values for lesions 1 cm or smaller than the other enhanced sequences, in contrast with the sensitivity results.

False-Negative Findings

At the confidence levels of 4 or 5, 16 lesions in 12 patients were not detected by any observer for any image sets. Of these 16 lesions, in 6 patients, 10 lesions were smaller than 1 cm (six, <5 mm). For image set (E) alone, 12 lesions (seven ≤1 cm) in 8 patients could be detected by at least one observer. Four lesions (three <1 cm) in 3 patients were observed by at least one observer with (B) alone and 2 lesions (one <1 cm) in 2 patients could be observed with (D) alone. With regard to false-negative lesions, blurring and motion artifacts were responsible for degrading image quality.

DISCUSSION

SPIO-enhanced MR imaging has been used to improve the detection and characterization of hepatic lesions. Gadolinium ethoxybenzyl diethylenetriaminepentaacetic acid (Gd-EOB-DTPA), a gadolinium-based contrast agent that targets hepatocytes, was reported to be an effective method for the detection of colorectal liver metastasis[22] and is currently under intensive investigation. Gadobenate dimeglumine (Gd-BOPTA)-enhanced delayed-phase imaging was also reported to have comparable diagnostic performance to SPIO-enhanced imaging for the detection of liver metastases, and had a better diagnostic performance than Gd-BOPTA-enhanced dynamic images in patients with liver metastasis.[23] However, another study showed that, when Gd-BOPTA-enhanced MR imaging was compared with SPIO-enhanced MR imaging, only

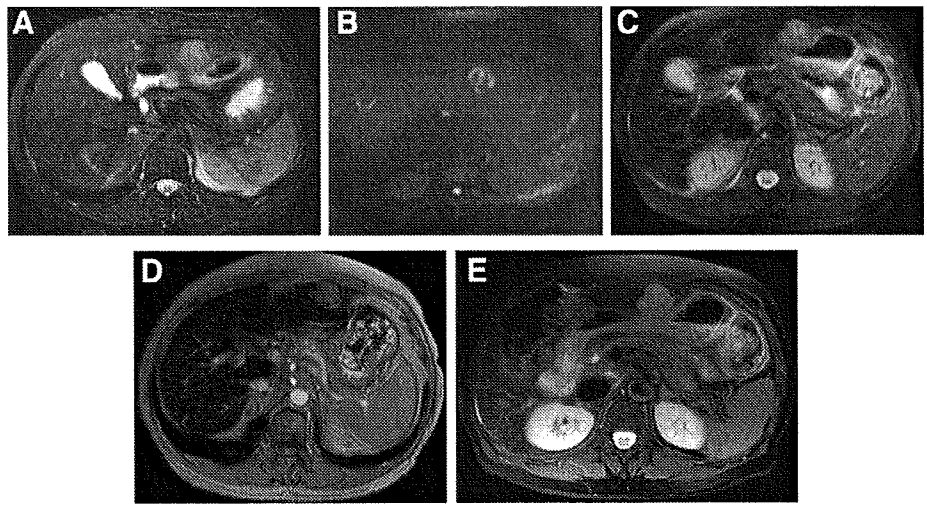

FIGURE 1. Images obtained using superparamagnetic iron oxide-enhanced (SPIO) administration obtained in a 55-year-old woman with hepatic metastasis from pancreatic cancer. Precontrast (A) fat-saturated T2-weighted TSE (5330/103), and (B) diffusion-weighted GRAPPA (2100/91; b-factor, 1000 seconds/mm^2) MR images. Postcontrast (C) fat-saturated T2-weighted TSE with respiratory triggering (PACE), (D) T2*-weighted GRE (169/9, 60 degrees flip angle), and (E) fat-saturated PROPELLER T2-weighted TSE with PACE MR images. A 3-cm diameter metastasis is seen in the lateral segment of the left lobe on all images. The patient is moving during the MR examination, and the hepatic lesion is the most clearly seen and given the best motion correction on the PROPELLER MR image (E). Some differences in slice position are observed because of respiration, although images were planned for the same position. Note that the hyperintense lesions in the right lobe (A, B, D) and in segment IV (C) were confirmed to be pseudo-lesions.

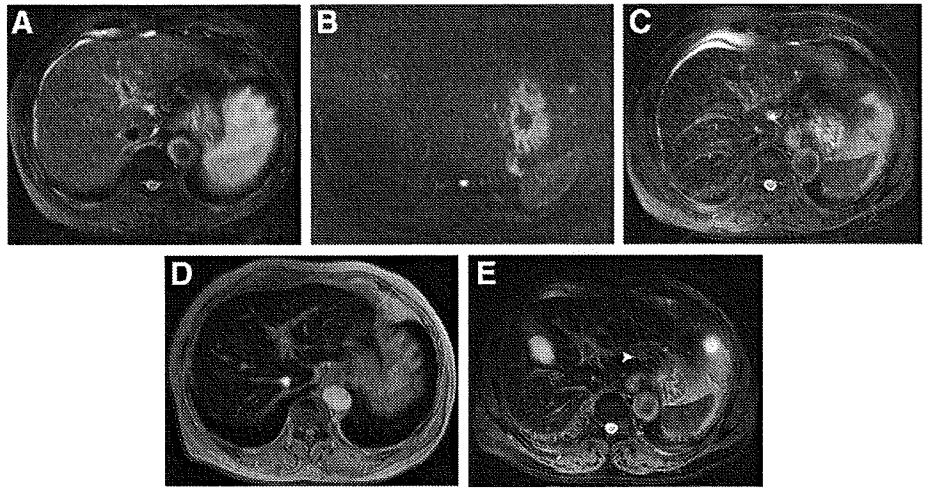

FIGURE 2. Abdominal images obtained using superparamagnetic iron oxide-enhanced (SPIO) administration in a 48-year-old man with pancreatic cancer. Precontrast (A) fat-saturated T2-weighted TSE (5330/103) and (B) diffusion-weighted GRAPPA (2100/91; b-factor, 1000 seconds/mm^2) MR images. Postcontrast (C) fat-saturated T2-weighted TSE with respiratory triggering (PACE), (D) T2*-weighted GRE (169/9, 60 degrees flip angle) and (E) fat-saturated PROPELLER T2-weighted TSE with PACE MR images. The hepatic metastatic lesion is obscure in all images except for that with the PROPELLER sequence (E) because of image artifacts. The 0.9-cm diameter hepatic tumor (arrowhead) in segment II can only be clearly observed using the PROPELLER method (E). Note that the hyperintense subcapsular lesions in segment IV (A, B) and in the right lobe (C, D) were confirmed to be pseudolesions.

SPIO-enhanced MRI was found to able to detect all liver metastases of less than 1 cm and was recommended for diagnosis of small colorectal liver metastases.[24] Therefore, improvements in SPIO-enhanced MRI remain an important technical issue. Hence, some physicians believe that SPIO-enhanced MR imaging is one of the most appropriate preoperative imaging procedures for the screening of hepatic metastases and shows high ability to differentiate between benign and malignant focal liver lesions on the basis of their cellular composition and function.[25] SPIO-enhanced MR imaging can be conducted in patients with advanced kidney disease who may develop nephrogenic systemic fibrosis as a result of gadolinium toxicity.[26,27]

Although various pulse sequences have been used by many investigators for SPIO-enhanced MR imaging, T2*-weighted GRE

sequences are regarded as an essential method to detect focal hepatic lesions.[25,28,29] A previous study reported that respiratory-triggered T2-weighted TSE images after SPIO administration provided greater tumor-to-liver contrast and subjective conspicuity for hepatic lesions.[30] However, motion artifacts caused by respiration, cardiovascular pulsation, peristalsis, and physical movement deteriorate abdominal MR image quality and prevented lesion detection.[31–33] To overcome these limitations, a recently introduced acquisition technique PROPELLER can be used instead. It has a theoretical advantage of central k-space oversampling,[11] which was reported to reduce motion-related image artifacts[20] as well as increase SNR[21] in clinical cases. The PROPELLER technique applied to the upper abdominal imaging improved the quality of T2-weighted TSE imaging.[10,18–21] Therefore, it was reasonable to hypothesize that fat-saturated T2-weighted TSE imaging with the PROPELLER technique in combination with SPIO administration may improve the detection of hepatic lesions compared with other sequences including diffusion-weighted imaging or SPIO-enhanced T2*-weighted GRE imaging.

The results of our study showed that the detection of hepatic lesions with the PROPELLER technique was superior to those with other sequences. In a previous study, MR imaging using the PROPELLER technique was shown to reduce image artifacts and image noise, resulting in better image quality in the upper abdomen.[18] This suggested the probability of improving the detection of hepatic lesions by adopting these methods. With the use of SPIO-enhanced sequences, the accuracy and sensitivity for the detection of hepatic lesions were higher than those of the unenhanced basic image set. Notably, the SPIO-enhanced MR sets using the T2*-weighted GRE sequence obtained during breath-hold was statistically better than fat-saturated T2-weighted TSE with PACE. This might be due to image artifacts caused by a mismatch in the respiratory rhythm or by and increased magnetization transfer saturation.[34,35] On the other hand, T2*-weighted GRE imaging may be affected by low SNR and susceptible artifacts.[36] The PROPELLER technique can offer motion correction to overcome these limitations.[37,38] About half of the hepatic metastases in the current study were equal to or smaller than 1 cm in size, and fat-saturated T2-weighted TSE imaging with PROPELLER was confirmed to show the highest sensitivity for these metastases.

Several reports showed the high ability for body diffusion-weighted images to detect various malignant tumors.[8,39–42] Diffusion-weighted MR imaging using high-b-value achieved detection of colorectal, pancreatic adenocarcinoma and focal liver masses with high sensitivity and specificity.[39,40,42] Combined reading of diffusion-weighted images and unenhanced T1/T2-weighted images (ie, the basic image set) had higher accuracy for the detection of hepatic metastases than SPIO-enhanced MR images.[8] In the present study, SPIO-enhanced MR sets using PROPELLER technique enabled improved detection of hepatic lesions 1 cm in diameter or smaller as well as lesions larger than 1 cm than the MR sets using diffusion-weighted images. There were some false-positive and false-negative lesions on the MR sets using diffusion-weighted images because of distortion and misregistration of fat tissue, image artifacts, and low resolution after combined interpretation of fat-saturated T2-weighted TSE images. The PROPELLER technique might be useful to detect hepatic lesions affected by image artifacts such as respiratory motion, cardiovascular pulsation, bowel movement, and physical movement that deteriorate MR image quality. However, 4 lesions (3 lesions smaller than 1 cm) were only detectable in the diffusion-weighted images and it has a certain contribution to improvement of diagnostic capability.

There are several potential limitations in our study. First, not all of the hepatic lesions were pathologically confirmed. However, typical clinical and laboratory findings, in combination with disease progression in follow-up images, clearly indicated malignancy. Second, the image acquisition time increased with the PROPELLER technique. It may improve SNR, but also requires time for motion correction. The use of techniques such as parallel acquisition might reduce the acquisition time. Third, the parameters associated with PROPELLER acquisition, such as echo train length, blade width and number of blades, were not investigated in this study and may not be fully optimized. Therefore, we should investigate the optimal PROPELLER MR imaging parameters in future studies. Fourth, diffusion-weighted MR imaging in combination with the PROPELLER technique was not applicable because of limited abilities of the apparatus used here. Finally, no ADC analysis was conducted in this study; however, it could be misleading[43] and we did not use it.

In summary, SPIO-enhanced MR imaging with the PROPELLER technique is likely to improve the detection of hepatic metastases from pancreatic cancer in comparison with diffusion-weighted MR imaging, fat-saturated T2WI without PROPELLER technique, or SPIO-enhanced T2*-weighted GRE imaging. Further clinical studies are required to evaluate abdominal MR imaging with the use of optimized PROPELLER methods.

REFERENCES

1. Bartolozzi C, Lencioni R, Donati F, et al. Abdominal MR: liver and pancreas. *Eur Radiol.* 1999;9:1496–1512.
2. Bartolozzi C, Cioni D, Donati F, et al. Focal liver lesions: MR imaging-pathologic correlation. *Eur Radiol.* 2001;11:1374–1388.
3. Kondo H, Kanematsu M, Hoshi H, et al. Preoperative detection of malignant hepatic tumors: comparison of combined methods of MR imaging with combined methods of CT. *Am J Roentgenol.* 2000;174:947–957.
4. Coenegrachts K, Orlent HO, ter Beek L, et al. Improved focal liver lesion detection: comparison of single-shot spin-echo echo-planar and superparamagnetic iron oxide (SPIO)-enhanced MRI. *J Magn Reson Imaging.* 2008; 27:117–124.
5. Soyer P, Levesque M, Caudron A, et al. MRI of liver metastases from colorectal cancer vs. CT during arterial portography. *J Comput Assist Tomogr.* 1993;17:67–74.
6. Heiken JP, Weyman PJ, Lee JK, et al. Detection of focal hepatic masses: prospective evaluation with CT, delayed CT, CT during arterial portography, and MR imaging. *Radiology.* 1989;171:47–51.
7. Semelka RC, Schlund JF, Molina PL, et al. Malignant liver lesions: comparison of spiral CT arterial portography and MR imaging for diagnostic accuracy, cost, and effect on patient management. *J Magn Reson Imaging.* 1996;1:39–43.
8. Nasu K, Kuroki Y, Nawano S, et al. Hepatic metastases: diffusion-weighted sensitivity-encoding versus SPIO-enhanced MR imaging. *Radiology.* 2006; 239:122–130.
9. Chow LC, Bammer R, Moseley ME, et al. Single breath-hold diffusion-weighted imaging of the abdomen. *J Magn Reson Imaging.* 2003;18:377–382.
10. Deng J, Miller FH, Salem R, et al. Multishot diffusion-weighted PROPELLER magnetic resonance imaging of the abdomen. *Invest Radiol.* 2006;41: 769–775.
11. Pipe JG. Motion correction with PROPELLER MRI: application to head motion and free-breathing cardiac imaging. *Magn Reson Med.* 1999;42:963–969.
12. Wintersperger BJ, Runge VM, Biswas J, et al. Brain magnetic resonance imaging at 3 Tesla using BLADE compared with standard rectilinear data sampling. *Invest Radiol.* 2006;41:586–592.
13. Fobes KP, Pipe JG, Bird CR, et al. PROPELLER MRI: clinical testing of a novel technique for quantification and compensation of head motion. *J Magn Reson Imaging.* 2001;14:215–222.
14. Fobes KP, Pipe JG, Karis JP, et al. Improved image quality and detection of acute cerebral infarction with PROPELLER diffusion-weighted MR imaging. *Radiology.* 2002;225:551–555.
15. Attenberger UI, Runge VM, Stemmer A, et al. Diffusion Weighted Imaging: A Comprehensive Evaluation of a Fast Spin Echo DWI Sequence With

BLADE (PROPELLER) k-Space Sampling at 3 T, Using a 32-Channel Head Coil in Acute Brain Ischemia. *Invest Radiol.* 2009;44:656–661.

16. Attenberger UI, Runge VM, Williams KD, et al. T1-Weighted Brain Imaging With a 32-Channel Coil at 3T Using TurboFLASH BLADE Compared With Standard Cartesian k-Space Sampling. *Invest Radiol.* 2009;44:177–183.
17. Deng J, Larson AC. Multishot targeted PROPELLER magnetic resonance imaging: description of the technique and initial applications. *Invest Radiol.* 2009;44:454–462.
18. Kiryu S, Watanabe M, Kabasawa H, et al. Evaluation of super paramagnetic iron oxide-enhanced diffusion-weighted PROPELLER T2-fast spin echo magnetic resonance imaging: preliminary experience. *J Comput Assist Tomogr.* 2006;30:197–200.
19. Hirokawa Y, Isoda H, Maetani Y, et al. MRI artifact reduction and quality improvement in the upper abdomen with the PROPELLER (BLADE) and navigator triggered prospective acquisition correction (PACE) technique. *Am J Roentgenol.* 2008;191:1154–1158.
20. Hirokawa Y, Isoda H, Maetani Y, et al. Evaluation of motion correction effect and image quality with the periodically rotated overlapping parallel lines with enhanced reconstruction (PROPELLER) (BLADE) and parallel imaging acquisition technique in the upper abdomen. *J Magn Reson Imaging.* 2008; 28:957–962.
21. Hirokawa Y, Isoda H, Maetani Y, et al. Hepatic lesions: improved image quality and detection with the periodically rotated overlapping parallel lines with enhanced reconstruction technique—evaluation of SPIO-enhanced T2-weighted MR images. *Radiology.* 2009;251:388–397.
22. Zech CJ, Grazioli L, Jonas E, et al. Health-economic evaluation of three imaging strategies in patients with suspected colorectal liver metastases: Gd-EOB-DTPA-enhanced MRI vs. extracellular contrast media-enhanced MRI and 3-phase MDCT in Germany, Italy and Sweden. *Eur Radiol.* 2009;19(suppl 3):S753–S763.
23. Kim YK, Lee JM, Kim CS, et al. Detection of liver metastases: gadobenate dimeglumine-enhanced three-dimensional dynamic phases and one-hour delayed phase MR imaging versus superparamagnetic iron oxide-enhanced MR imaging. *Eur Radiol.* 2005;15:220–228.
24. Hekimoglu K, Ustundag Y, Dusak A, et al. Small colorectal liver metastases: detection with SPIO-enhanced MRI in comparison with gadobenate dimeglumine-enhanced MRI and CT imaging. *Eur J Radiol.* 2009;Sep 23. [Epub ahead of print].
25. Namkung S, Zech CJ, Helmberger T, et al. Superparamagnetic iron oxide (SPIO)-enhanced liver MRI with ferucarbotran: efficacy for characterization of focal liver lesions. *J Magn Reson Imaging.* 2007;25:755–765.
26. Cowper SE. Nephrogenic system fibrosis: the nosological and conceptual evolution of nephrogenic fibrosing dermopathy. *Am J Kidney Dis.* 2005;46: 763–765.
27. Perez-Rodriguez J, Lai S, Ehst BD, et al. Nephrogenic systemic fibrosis: incidence, associations, and effect of risk factor assessment—report of 33 cases. *Radiology.* 2009;250:371–377.
28. Kanematsu M, Ito K, Matsuo M, et al. Malignant hepatic tumor detection with ferumoxides-enhanced MR imaging with a 1.5-T system: comparison of four imaging pulse sequences. *J Magn Reson Imaging.* 2001;13:249–257.
29. Kim MJ, Kim JH, Choi JY, et al. Optimal TE for SPIO-enhanced gradient-recalled echo MRI for the detection of focal hepatic lesions. *Am J Roentgenol.* 2006;187:W255–W266.
30. Ishiyama K, Hashimoto M, Izumi J, et al. Tumor-liver contrast and subjective tumor conspicuity of respiratory-triggered T2-weighted fast spin-echo sequence compared with T2*-weighted gradient recalled-echo sequence for ferucarbotran-enhanced magnetic resonance imaging of hepatic malignant tumors. *J Magn Reson Imaging.* 2008;27:1322–1326.
31. Wood ML, Henkelmann RM. MR image artifacts from periodic motion. *Med Phys.* 1985;12:143–151.
32. Haacke EM, Patric JL. Reducing motion artifacts in two-dimensional Fourier transform imaging. *Magn Reson Imaging.* 1986;4:359–376.
33. Yang W, Smith MR. Using an MRI distortion transfer function to characterize the ghosts in motion-corrupted images. *IEEE Trans Med Imaging.* 2000;19: 577–584.
34. Abe Y, Yamashita Y, Namimoto T, et al. The value of fast and ultrafast T2-weighted MR imaging sequences in hepatic enhancement with ferumoxides: comparison with conventional spin-echo sequence. *Radiat Med.* 2000; 18:97–105.
35. Ward J, Guthrie JA, Wilson D, et al. Colorectal hepatic metastases: detection with SPIO-enhanced breath-hold MR imaging-comparison of optimized sequences. *Radiology.* 2003;228:709–718.
36. Abe Y, Yamashita Y, Namimoto T, et al. The value of fast and ultrafast T2-weighted MR imaging sequences in hepatic enhancement with ferumoxides: comparison with conventional spin-echo sequence. *Radiat Med.* 2000; 18:97–105.
37. Tanimoto A, Yuasa Y, Shinmoto H, et al. Superparamagnetic iron oxide-mediated hepatic signal intensity change in patients with and without cirrhosis: pulse sequence effects and Kupffer cell function. *Radiology.* 2002;222: 661–666.
38. Yoshikawa T, Mitchell DG, Hirota S, et al. Gradient- and Spin-echo T2-weighted imaging for SPIO-enhanced and characterization of focal liver lesions. *J Magn Reson Imaging.* 2006;27:712–719.
39. Ichikawa T, Erturk SM, Motosugi, et al. High-b-value diffusion-weighted MRI in colorectal cancer. *Am J Roentgenol.* 2006;187:181–184.
40. Ichikawa T, Erturk SM, Motosugi, et al. High-b-value diffusion-weighted MRI for detecting pancreatic adenocarcinoma. *Am J Roentgenol.* 2007;187: 409–414.
41. Tsushima Y, Takano A, Taketomi A, et al. Body diffusion-weighted MR imaging high b-value for malignant tumor screening: usefulness and necessity of referring to T2-weighted images and creating fusion imaging. *Acad Radiol.* 2007;14:643–650.
42. Erturk SM, Ichikawa T, Sano K, et al. Diffusion-weighted magnetic resonance imaging for characterization of focal liver masses: impact of parallel imaging (SENSE) and b value. *J Comput Assist Tomogr.* 2008;32:865–871.
43. Uto T, Takehara Y, Nakamura Y, et al. Higher sensitivity and specificity for diffusion-weighted imaging of malignant lung lesions without apparent diffusion coefficient quantification. *Radiology.* 2009;252:247–254.

European Journal of Radiology xxx (2009) xxx–xxx

Contents lists available at ScienceDirect

European Journal of Radiology

journal homepage: www.elsevier.com/locate/ejrad

The potential clinical value of FDG-PET for recurrent renal cell carcinoma

Koya Nakatani[a,*], Yuji Nakamoto[a,1], Tsuneo Saga[b,2], Tatsuya Higashi[c,3], Kaori Togashi[a,4]

[a] Department of Diagnostic Imaging and Nuclear Medicine, Kyoto University Graduate School of Medicine, 54 Shogoin-kawahara-cho, Sakyo-Ku, Kyoto 606-8507 Japan
[b] Department of Diagnostic Imaging Molecular Imaging Center, National Institute of Radiological Sciences, 4-9-1 Anagawa, Inage-Ku, Chiba 263-8555, Japan
[c] Research Institute, Shiga Medical Center for Adults, 5-4-30 Moriyama, Moriyama City, Shiga 524-8524 Japan

ARTICLE INFO

Article history:
Received 4 September 2009
Received in revised form
19 November 2009
Accepted 19 November 2009

Keywords:
^{18}F-FDG-PET
Renal cell carcinoma
Recurrence
Prognostic value

ABSTRACT

Purpose: The clinical value of positron emission tomography (PET) using ^{18}F-fluorodeoxyglucose (FDG) for follow-up or suspected recurrence of renal cell carcinoma (RCC) has not been fully evaluated. The purpose of this study was to assess the diagnostic performance of FDG-PET for postoperative assessment in patients with RCC.
Methods: We reviewed 28 scans in 23 patients who had undergone FDG-PET scans after surgery for RCC. Diagnostic accuracy of visually interpreted PET was evaluated based on final diagnoses obtained histologically or by clinical follow-up at least 6 months. Also, additional information over CT, influence on treatment decisions, and the accuracy of FDG uptake as a predictor of survival were assessed.
Results: Recurrence of renal carcinoma was histologically ($n = 15$) or clinically ($n = 6$) confirmed in 21 of 28 cases. Overall, the sensitivity, specificity, and diagnostic accuracy using FDG-PET were 81%, 71%, and 79%, respectively. In papillary RCC, the sensitivity was 100%; however, that was 75% in clear cell RCC in patient-basis. PET correctly detected local recurrence and metastases in all cases in the peritoneum, bone, muscle and adrenal gland. Additional information was obtained from scans in 6 cases (21%), which influenced therapeutic management in 3 cases (11%). Cumulative survival rates over 5 years in the PET-positive vs. the PET-negative group were 46% vs. 83%, respectively ($p = 0.17$).
Conclusions: FDG-PET would be useful for postoperative surveillance in patients with RCC, although its impact on treatment decisions may be limited. Further investigations are necessary to conclude whether PET has a prognostic value.

1. Introduction

Positron emission tomography (PET) with ^{18}F-fluorodeoxyglucose (FDG) has been widely used in clinical oncology as an established modality for imaging cancer. FDG-PET is applicable especially for staging or re-staging, and monitoring therapeutic response in several cancers. As for renal cell carcinoma (RCC), Wahl et al. reported the feasibility of metabolic imaging using FDG, as well as morphological imaging for primary and metastatic tumors in their pilot study in 1991 [1], followed by reports describing high accuracy of FDG-PET for the diagnosis of RCC [2–4]. Conversely, other reports have indicated higher false-negative rates [5,6]. Kang et al. examined 90 PET scans in 66 patients, and concluded that the role of FDG-PET in the detection of RCC was limited due to its low sensitivity and that, with superior specificity; PET might have a complementary role as a problem-solving tool in cases that were equivocal using conventional imaging [7]. Thus, the clinical role of FDG-PET for RCC remains controversial, but has not been considered helpful for the evaluation of primary RCC.

Meanwhile, the role of FDG-PET for follow-up or suspected recurrence of RCC has been reported to be favorable [8–10]. Clinical courses in patients with recurrent RCC following nephrectomy vary, with a survival benefit associated with sufficient metastasectomy [11–15]. More accurate diagnosis of recurrent RCC is important, but morphological imaging modalities, such as computed tomography (CT), have certain limitations for exact evaluation of recurrent RCC. Hence, metabolic imaging, including FDG-PET, is expected to demonstrate increased accuracy, but not much has been reported yet on the efficacy of PET in the diagnosis of recurrent RCC.

In the present study, to elucidate the clinical value of FDG-PET for recurrence and distant metastases of RCC, we assessed diagnostic performance of FDG-PET for postoperative survey in patients with RCC. Furthermore, we assessed whether FDG uptake could be a predictor of survival in patients with recurrent RCC.

* Corresponding author. Tel.: +81 75 751 3419; fax: +81 75 771 9709.
E-mail addresses: koyakn@kuhp.kyoto-u.ac.jp (K. Nakatani), 9709.ynakamo1@kuhp.kyoto-u.ac.jp (Y. Nakamoto), saga@nirs.go.jp (T. Saga), higashi@shigamed.jp (T. Higashi), ktogashi@kuhp.kyoto-u.ac.jp (K. Togashi).
[1] Tel.: +81 75 751 3762; fax: +81 75 771 9709.
[2] Tel.: +81 43 206 3429.
[3] Tel.: +81 77 582 6034; fax: +81 77 582 6041.
[4] Tel.: +81 75 751 3760; fax: +81 75 771 9709.

0720-048X/$ – see front matter © 2009 Elsevier Ireland Ltd. All rights reserved.
doi:10.1016/j.ejrad.2009.11.019

Please cite this article in press as: Nakatani K, et al. The potential clinical value of FDG-PET for recurrent renal cell carcinoma. Eur J Radiol (2009), doi:10.1016/j.ejrad.2009.11.019

2. Patients and methods

2.1. Patients

Between August 2000 and January 2008, 39 patients underwent 45 FDG-PET scans at our institute in order to investigate RCC. Among them, 8 patients (undergoing 8 scans) did not histologically prove to have RCC because they did not undergo surgery or biopsy, 1 patient (undergoing 1 scan) had bilateral renal tumors, one of which was not histologically proven, and 6 patients (undergoing 7 scans) had synchronous double cancer. These patients were excluded in our study. In this retrospective study, we reviewed records of 24 patients (18 men, 6 women; age range: 45–78 years, mean age: 63 years) who had histopathologically proven RCC and did not have synchronous malignant tumors. They underwent 29 PET scans. Periods from prior nephrectomy to PET scan ranged from 1 month to 27 years (average: 7.6 years, median: 3.5 years). All cases underwent both PET and CT scans and had prior CT scans. Each scan was performed within 6 months (18 scans within a month). All these studies involved daily clinical diagnostic checkups and written informed consent, requested by our institutional review board, was obtained from each patient.

2.2. PET scanning

Fluorine-18 FDG was synthesized by nucleophilic substitution method using an FDG synthesizing instrument (F-100, Sumitomo Heavy Industries, Tokyo, Japan) and a cyclotron (CYPRIS-325R, Sumitomo Heavy Industries, Tokyo, Japan). For 22 patients (27 scans) in this study, PET was performed using an Advance scanner (GE Healthcare, Milwaukee, WI, USA). For the remaining 2 patients (2 scans), PET was performed using a C-PET plus scanner (ADAC, Philadelphia, PA, USA). After fasting for at least 4 h, patients received intravenous administration of approximately 370 MBq (for the Advance scanner) or 130 MBq (for the C-PET plus scanner) of FDG, and whole-body PET images were acquired approximately 60 min later. Using the Advance scanner, each emission scan was obtained for 3 min per single bed position and each post-emission transmission scan was obtained for 1 min per single bed position. In order to cover from the skull base to the upper thigh, 5–6 bed positions were scanned according to the height of each patient. Images were acquired in 2-dimensional mode. The ordered subset expectation maximization algorithm using 16 subsets, 3 iterations, and a 128 × 128 matrix size reconstructed attenuation-corrected transaxial images. Data acquisition by the C-PET plus scanner was performed in 3-dimensional imaging mode with septae in place. Following a 56-s transmission scan, a whole body static image was then acquired for 6 min per bed position. The data were reconstructed using row action maximum likelihood algorithm.

2.3. CT scanning

CT scans were performed prior to PET scans using single or multidetector-row CT scanners (Aquillion 8, 16, or 64, Toshiba, Tokyo, Japan; W3000, Hitachi Medico, Tokyo, Japan; HiSpeed Advantage, GE Healthcare, Milwaukee, WI, USA). Thoracic and abdominal images were obtained separately or continuously with (19 scans) or without (10 scans) intravenous contrast material.

Table 1
Characteristics, results of images, and clinical outcomes of patients with RCC.

Pt. #	Age/Sex	Histology of prior specimen[a]			Result		Sites of metastases		Outcome
		Type	Grade	TNM	CT	PET	P/o by PET	Final Dx	
1	57/M	CCC	NA	NA	TP	TP	Lu	*Lu*	Rec.
	58/M				TN	FP	(Lu)[c]	None	Rec.
	60/M				TN	TN	None	None	Rec.
	61/M				FN	TP	LN	*LN*	No rec.
	62/M				TN	TN	None	None	No rec.
2	69/M	CCC	1	T3b	TN	TN	None	None	No rec.
3	54/M	CCC	2	T2a	FP	FP	(LN)[c]	None	No rec.
4	65/M	CCC	1	T2b	FP	TN	None	None	No rec.
5	76/M	CCC	2	T1a	TP	TP	Bo	Bo	Drop out (rec.)
	77/M				TP	TP	Bo	Bo, Lu	Drop out (rec.)
6	46/M	CCC	3	Tx	TP	TP	Ki, LN, Pe	Ki, LN, *Pe*	Death
7	52/M	CCC[b]	3	M1	TP	FN	None	Br, Lu	Rec.
8	77/M	CCC	2	T2	TP	TP	Bo, LN, Lu, Mu	Bo, Lu, LN, Mu, *Sk*	Death
9	62/M	CCC[b]	3	M1	TP	TP	Lu, Ad	Ad, Br, Lu	Death
10	58/M	PRC	2	T1a	TP	TP	Pe	Pe	Death
11	71/F	CCC[b]	3	T3b	TP	TP	Ad, Lo, Mu	Ad, Lo, *Mu*	Death
12	59/M	CCC	NA	NA	TP	TP	Pa	*Pa*	No rec.
13	58/M	CCC[b]	3	T1b	TP	FN	None	Ki, Pa, Thy	Rec.
14	73/F	CCC	NA	NA	TP	TP	Pa	*Pa*	No rec.
15	65/M	CCC	1	T2b	TP	TP	Pa	*Pa*	Drop out (rec.)
16	56/M	CCC	NA	T2	TP	FN	None	*Pa*	No rec.
17	66/M	PRC	3	M1	FN	TP	Bo	Bo	Death
18	54/F	PRC	3	M1	TP	TP	Ad, Bo, Lu	Ad, Bo, Lu	Death
19	78/M	NA	3	T1a	TP	TP	Lu	Lu	No rec.
20	45/F	PRC	2	T3b	TP	TP	Bo, LN, Lo, Mu	Bo, LN, Lo, *Mu*	Death
21	56/F	CCC	NA	NA	TP	FN	None	*Li*	Death
22	75/F	CCC	2	T1b	TN	TN	None	None	Death from pneumonia
23	64/M	CCC	3	M1	TP	TP	Bo, Li	Bo, *Li*	Drop out (rec.)

Abbreviations: Pt. #, patient number; F, female; M, male; CCC, clear cell carcinoma; PRC, papillary renal cell carcinoma; NA, not available; TP, true positive; TN, true negative; FP, false positive; FN, false negative; P/o, pointed out; Dx, diagnosis; Ad, adrenal gland; Bo, bone; Br, brain; Ki, contralateral kidney; Li, liver; LN, lymph node; Lo, local recurrence; Lu, lung; Mu, muscle; Pa, pancreas; Pe, peritoneal dissemination; Sk, skin; Thy, thyroid; Rec., recurrence.
Sites of metastases written in *oblique type* were biopsy-proven, and sites of metastases written in *oblique type and underlined* were surgically proven.
[a] Histological findings are based on the 3rd edition of the General Rule for Clinical and Pathological Studies on Renal Cell Carcinoma (in Japanese).
[b] With sarcomatoid component.
[c] False-positive lesion.

Please cite this article in press as: Nakatani K, et al. The potential clinical value of FDG-PET for recurrent renal cell carcinoma. Eur J Radiol (2009), doi:10.1016/j.ejrad.2009.11.019

2.4. Image interpretation and analysis

Interpretations of PET images were performed by consensus of at least two nuclear medicine physicians, with all available clinical information, including anatomical information provided by prior CT and/or other conventional imaging modalities. In this study, interpretation criteria were as follows; lesions were regarded as being an abnormal finding or representative of tumor if metabolic activity of FDG was moderately or markedly increased, relative to comparable normal structures or surrounding soft tissues. Findings provided by CT images, such as lesion size, shape, or enhancement patterns, were not taken into account for the purpose of the study. For example, a lesion with no or faint uptake of FDG was regarded as negative even if a recurrent tumor had been suspected by CT. Based on these criteria, the diagnostic accuracy of PET was estimated. Final diagnoses were made histopathologically or according to clinical follow-up using CT scans for at least 6 months.

When PET detected lesions that had not been observed by conventional imaging modalities, or when PET revealed characteristics of lesions other modalities interpreted inconclusively, the obtained finding was regarded as '*additional information*'. If patient treatments changed as a result of PET findings, these findings were considered to have offered '*clinical impact*'.

Patients were categorized into a PET-positive and a PET-negative group. Kaplan–Meier survival estimates were calculated from the first day of the PET scan to death.

3. Results

We evaluated a total of 28 PET scans in 23 patients and excluded 1 patient (using the Advance scanner) without definite final diagnosis. The patients' profile and their clinical outcome are shown in Table 1. Of 28 cases, 21 were finally confirmed to be in recurrence via surgery ($n = 7$), biopsy ($n = 8$), and clinical follow-up ($n = 6$), i.e. the tumor had increased in size. The remaining 7 cases were considered negative for recurrence. Histopathology demonstrated that the type of recurrent cases were clear cell RCC in 16 patients, papillary RCC in 4 patients, and unknown in 1 case.

The PET results were true-positives in 17 cases (clear cell RCC in 12 cases, papillary RCC in 4 cases, and unknown histology in 1 case). Fig. 1 demonstrates a true-positive case which gave additional information and clinical impact. On the other hand, PET failed to show recurrent lesions in 4 cases, all of which were clear cell RCC. These missed observations included 1 case of brain and lung metastases, 1 case of multiple small liver metastases, and 2 cases of metastases to the pancreas. Fig. 2 demonstrates 1 representative false-negative case. PET findings yielded false positive in 2 cases. One case revealed inflammatory changes in the lung and the other, mediastinal lymphadenitis. In the remaining 5 cases, the results of PET scans were true negative. As shown in Table 2, overall sensitivity, specificity, accuracy, positive predictive value, and negative predictive value were 81%, 71%, 79%, 90%, and 56%, respectively. When objects were confined to the cases with clinically suspected recurrence by prior CT images or by clinical symptoms, such as general malaise or long-lasting fever, the sensitivity, specificity,

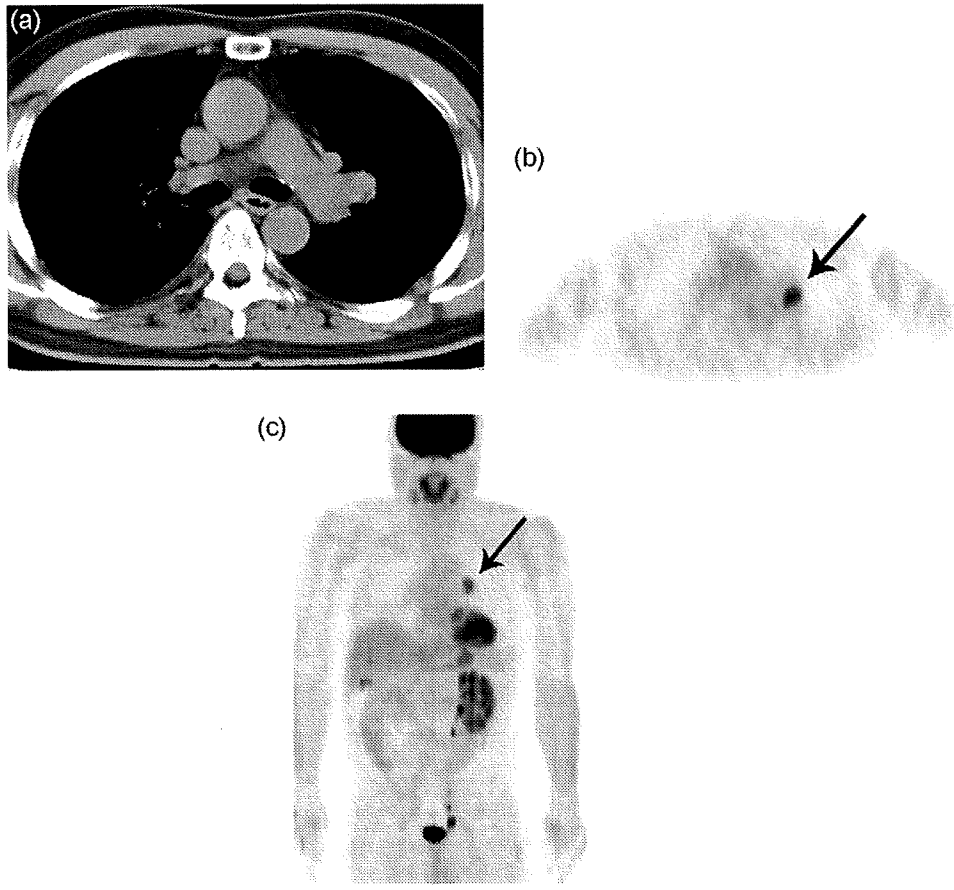

Fig. 1. A case of true-positive FDG-PET for metastatic renal cell carcinoma with additional information and clinical impact. An axial slice of unenhanced CT (a) and an axial slice (b) and maximum intensity projection (MIP) image (c) of FDG-PET are shown. A 61-year-old male (Pt. #1) respectively had a history of right nephrectomy and pulmonary metastasectomy 16 and 3 years earlier. He underwent unenhanced CT and no more lesions were found. PET showed significant uptake on the left hilar lymph node (arrows), indicating metastasis to the lymph node. Surgical resection was performed, and the lesion turned out to be a positive node.

Please cite this article in press as: Nakatani K, et al. The potential clinical value of FDG-PET for recurrent renal cell carcinoma. Eur J Radiol (2009), doi:10.1016/j.ejrad.2009.11.019

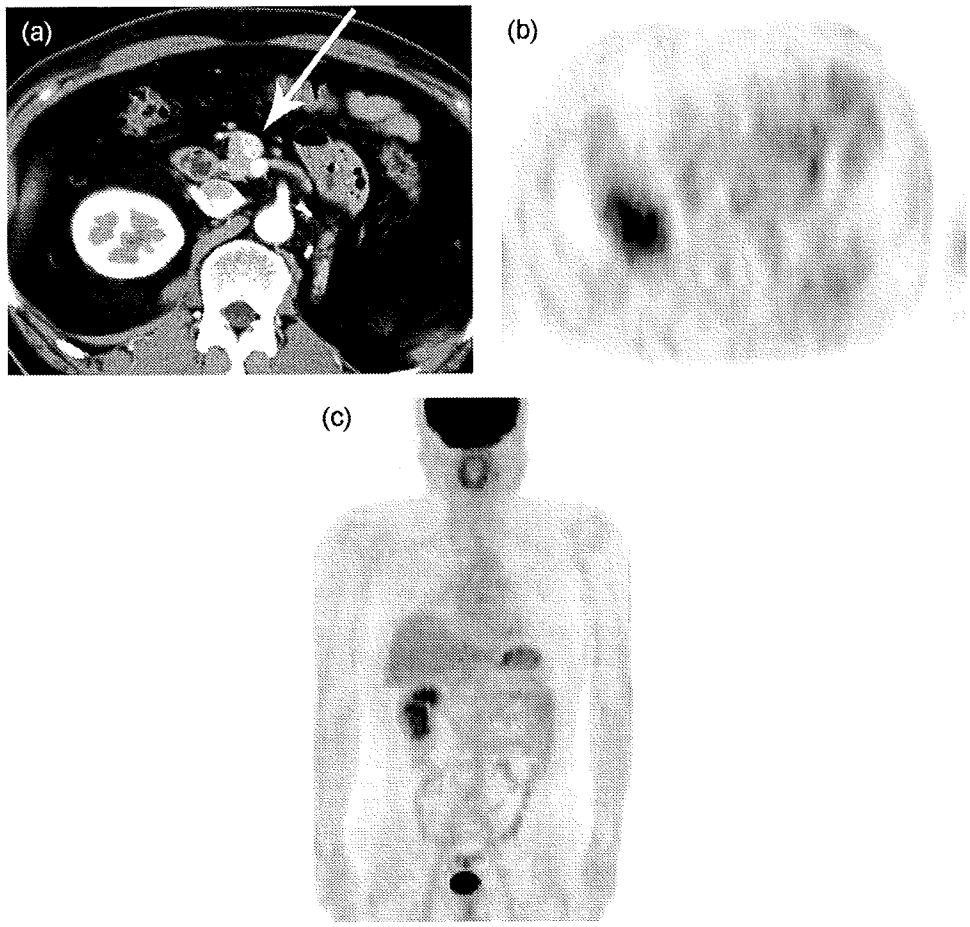

Fig. 2. A case of false-negative FDG-PET for metastatic renal cell carcinoma. An axial slice of arterial phase of enhanced CT (a) and an axial slice (b) and maximum intensity projection image (c) of FDG-PET are shown. A 56-year-old male (Pt. #16) underwent CT and was suspected of having metastasis. FDG-PET showed no significant uptake. The tumor was resected, and metastasis to the pancreas was histologically confirmed.

Table 2a
Cross-tabulation of the results of case-based analysis ($n = 28$).

		Final diagnosis	
		Recurrence (+)	Recurrence (−)
PET	Positive	17	2
	Negative	4	5

Sensitivity 81%, specificity 71%, accuracy 79%.

accuracy, positive predictive value, and negative predictive value of PET were 80%, 67%, 78%, 94%, and 33%, respectively.

All 4 false-negative cases had clear cell RCC, and the PET results in all 4 cases with papillary RCC were true-positive. However, there was no statistically significant difference about the diagnostic accuracy between the two histological subtypes according to Fisher's exact test ($p = 0.5376$). No correlation was found between nuclear grades of primary tumors and FDG uptake of recurrent tumors, either.

Table 2b
Cross-tabulation of the results of cases with suspected recurrence ($n = 23$).

		Final diagnosis	
		Recurrence (+)	Recurrence (−)
PET	Positive	16	1
	Negative	4	2

Sensitivity 80%, specificity 67%, accuracy 78%.

PET correctly detected local recurrence, peritoneal dissemination, bone metastases, muscle metastases, and adrenal metastases in all cases. On the other hand, sensitivities of metastases to the brain, thyroid, liver, or contralateral kidney were low, although the number of metastatic lesions was limited (Table 3). Fig. 3 demonstrates a case with metastases to the peritoneum and kidney.

'Additional information' over CT was obtained in 6 cases (21%). In 1 patient (No. 1), who had been thought to be disease-free by prior unenhanced CT, PET revealed a hilar lymph node metastasis which was confirmed histologically. In another patient (No. 17), whose prior CT image investigating the cause of general malaise

Table 3
Number of cases according to metastatic foci.

Metastatic organ	No. of total cases	No. of PET true-positive cases
Lung	7	5 (71.4%)
Mediastinal lymph node	3	2 (66.6%)
Abdominal lymph node	2	2 (100%)
Bone	7	7 (100%)
Contralateral kidney	2	1 (50%)
Brain	2	0 (0%)
Pancreas	5	3 (60%)
Adrenal gland	3	3 (100%)
Peritoneal dissemination	2	2 (100%)
Muscle	3	3 (100%)
Local recurrence	2	2 (100%)
Skin	1	0 (0%)
Liver	2	1 (50%)
Thyroid	1	0 (0%)

Please cite this article in press as: Nakatani K, et al. The potential clinical value of FDG-PET for recurrent renal cell carcinoma. Eur J Radiol (2009), doi:10.1016/j.ejrad.2009.11.019

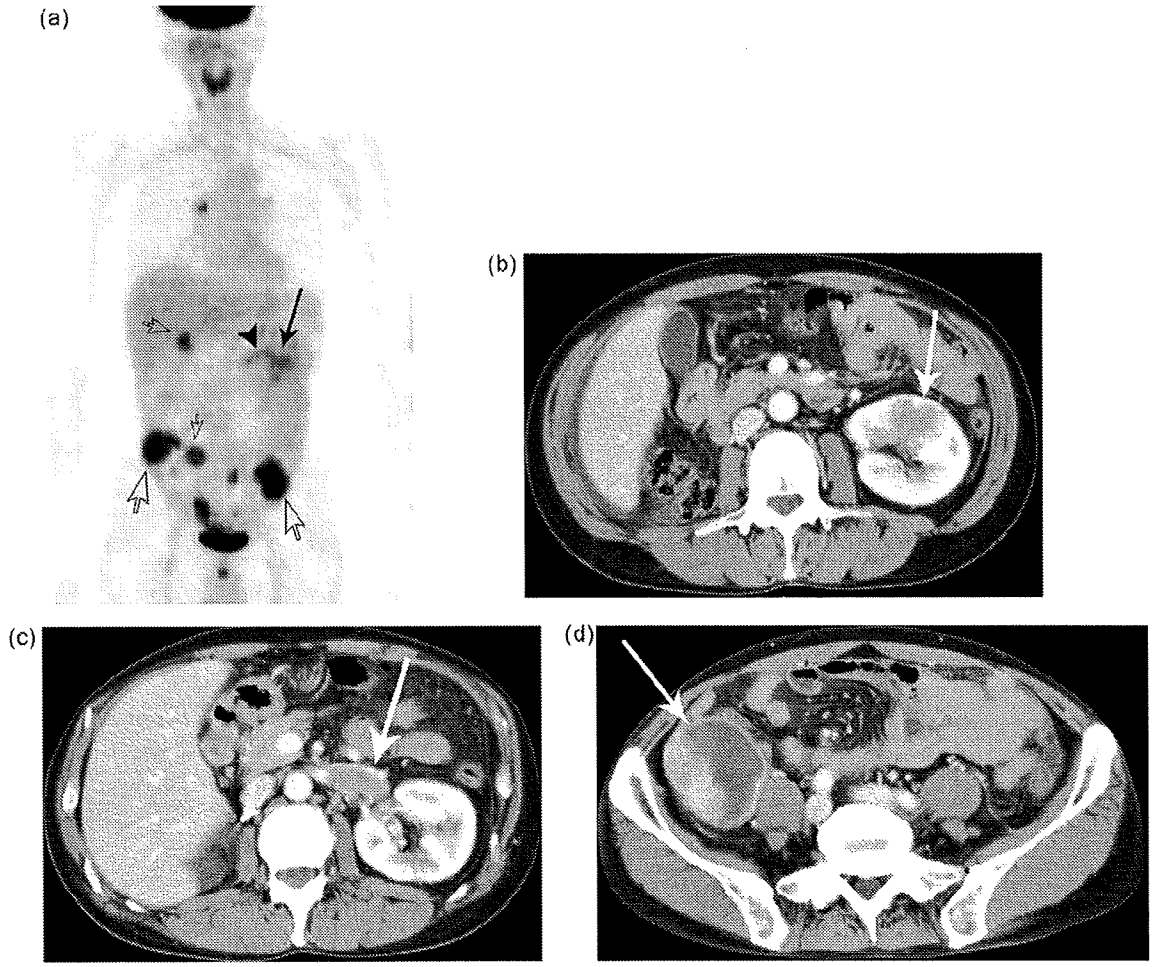

Fig. 3. A case with metastatic renal cell carcinoma to the peritoneum, right hilar nodes, and left kidney. A maximum intensity projection image of FDG-PET (a) and axial slices of enhanced CT (b–d) are demonstrated. Metastatic lesions to the contralateral kidney (a: black arrow, b: white arrow) and to the peritoneum (a, d: white arrows) were identified as FDG-avid foci. Tumor thrombus in the left renal vein is also seen on PET and CT (a: arrowhead, c: white arrow).

has not shown any remarkable findings, PET showed diffuse bone marrow metastases that were later biopsy-proven. In patient No. 20, PET discovered an unknown chest wall metastasis on her back, for which excision and irradiation therapy was performed. For these 3 patients, the PET findings were considered to yield 'clinical impacts'. In the remaining 3 patients, PET additionally revealed an adrenal gland metastasis, a sternal bone metastasis, and vertebral metastases, but their clinical management did not change.

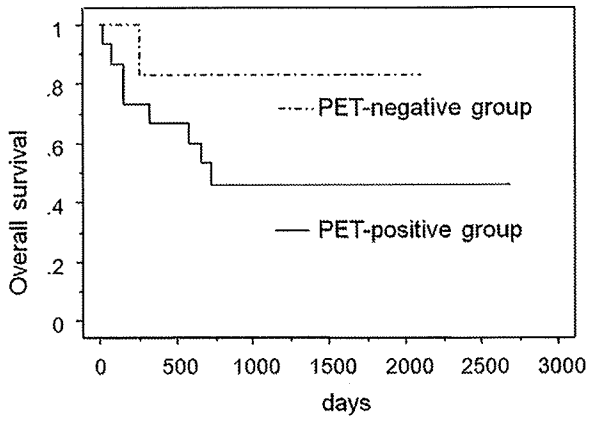

Fig. 4. The overall survival of the PET-positive group including 16 patients (solid line) and the PET-negative group including 6 patients (dashed line). The PET-positive group tended to have a poorer prognosis, but was not statistically significantly different ($p = 0.1739$).

Among the 23 patients for whom final diagnoses were obtained, 1 female patient died of pneumonia irrelevant to cancer. The survival analysis was, therefore, performed after excluding this patient. During their follow-up periods, ranging from 6 to 2691 days with the median of 711 days, 9 patients died of primary disease. Of these patients, 8 belonged to the PET-positive group (16 patients) and 1 patient, who died of liver failure due to multiple liver metastases, belonged to the PET-negative group (6 patients). Cumulative survival rates over 5 years in the PET-positive group and in the PET-negative group were 46% and 83%, respectively, as presented by Kaplan–Meier survival curves (Fig. 4). The difference between the two groups did not reach statistical significance according to the log-rank test ($\chi^2 = 1.849$, $p = 0.1739$).

4. Discussion

The overall diagnostic performance of FDG-PET for recurrent RCC after nephrectomy was reasonably high, with a case-based sensitivity of 81%, specificity of 71%, and accuracy of 79%, which was considered comparable with those for other malignancies. These data indicate that FDG-PET would be a useful tool for postoperative surveillance even in patients with RCC.

Please cite this article in press as: Nakatani K, et al. The potential clinical value of FDG-PET for recurrent renal cell carcinoma. Eur J Radiol (2009), doi:10.1016/j.ejrad.2009.11.019

The role of FDG-PET for re-staging of RCC was initially examined by Safaei et al., who examined 36 patients and demonstrated the sensitivity, specificity, and accuracy of 87%, 100%, and 89%, respectively [8]. According to published reports, overall sensitivity and specificity of FDG-PET for re-staging were 64–87% and 75–100% [8–10]. Our data were almost consistent with these observations. As for initial diagnosis and staging of primary RCC, overall sensitivity of FDG-PET varied, ranging from 32% to 100% [1–7]. The largest study by Kang et al. showed a sensitivity of 60% [7], raising questions as to the clinical value of FDG-PET. FDG-PET may be helpful in the evaluation of recurrent RCC rather than in initial staging of RCC.

In general, there are many RCC that are not FDG-avid, with the reason behind this phenomenon remaining unclear. For example, Miyauchi et al. reported that renal cancers in their series of 11 patients with newly diagnosed RCC were well visualized with FDG-PET, had higher grade, higher glucose transporter-1 (GLUT-1) expression and tended to be larger than poorly imaged cancers (Miyauchi T et al., presented at the 1996 annual meeting of the Society of Nuclear Medicine).

In contrast, Miyakita et al. stated that there was no correlation between GLUT-1 expression and FDG-PET positivity [5]. Montravers et al. formulated the hypothesis that mild or absent FDG contrast observed in primary RCC was due to a lack of accessibility of radiotracers to tumor cells [3,16].

As compared with primary tumors, it seems that recurrent or metastatic foci of RCC tended to be FDG-avid, resulting in higher sensitivity of FDG-PET, although a few recurrent tumors were not FDG-avid. In our study, uptake of FDG in recurrent tumors was not statistically correlated with histological type, nuclear grade, or presence of sarcomatoid components, as it is demonstrated in Table 1. This might be because of the small number of cases. Further examination with increased number of cases with various histological types might be needed. One of the reasons explaining the difference in the diagnostic performance could be attributed to the urinary system. FDG is excreted into urine yielding substantial tracer accumulation in a renal collecting system, and thus accumulation in primary RCC is sometimes obscured by or misrecognized as excretion itself [2,8,17]. FDG accumulation in metastatic tumors is not obscured by excretion, except in the contralateral kidney. Physiological uptake of FDG in background tissue can mask accumulation into tumors in liver, brain, and kidney. In fact, tumors metastasized to these organs tended to be missed in our population, although the number of the lesions was limited. Nevertheless, as shown in Fig. 3, there was a case in which a metastasis to kidney was identified because of FDG uptake in the tumor thrombus directly invading to a renal vein that could be easily distinguished from urinary tract.

Understanding how often additional information is obtained if FDG-PET is used in conjunction with morphological information, usually acquired by CT, is important in assessing the clinical utility of this technique. In our study, 'additional information' over CT was obtained in 6 cases (21%), causing an alteration of therapeutic plans in 3 of these cases (11%). Among these cases, 2 patients (7%) who had been regarded as disease-free by prior CT turned out to have recurrence that was detected using PET. However, several reports noted that metastasectomy under the appropriate conditions can bring survival benefits in selected patients [11–15]. A tumor-free interval of more than 2 years between primary tumor and metastasis was reported to be accompanied by a longer disease-specific survival after successful metastasectomy [11]. Moreover, molecular-targeted therapies with multi-kinase inhibitors such as sorafenib and sunitinib are now recommended as preferential therapy against metastatic RCC. Therefore, it is essential for starting these strategies to point out correct metastatic sites. In addition, there are no reliable specific tumor markers for RCC, although erythrocyte sedimentation rate (ESR), C-reactive protein (CRP), and serum immunosuppressive acidic protein (IAP) have been proposed to be a prognostic factor [18–20]. Therefore, the diagnostic imaging for evaluation of recurrence, including FDG-PET, may be helpful, even if clinical impacts cannot be obtained very frequently. Indeed, although postoperative surveillance is generally performed using CT, patients with renal insufficiency after nephrectomy are not permitted to perform CT with IV contrast material. CT without IV contrast provides limited information in pointing out unexpected metastases. Since renal carcinomas have a tendency to metastasize to a variety of organs, it would be difficult to detect metastases to pancreas or muscle only by unenhanced CT. Especially in these cases, we believe that FDG-PET (or PET/CT) can be effectively applicable.

In survival time analysis, the PET-positive group tended to have poorer prognosis, but the difference of cumulative survival rates between the two groups did not reach statistical significance. One of the reasons might be the small number of cases. We need to perform a further investigation using an increased number of cases to conclude prognostic value of FDG-PET for recurrent RCC. In addition, the kind of adjuvant therapy the patients received, or whether metastatic tumors were successfully removed after being found, was not taken into account in the present analysis. Survival curves for both the PET-positive and PET-negative group were ultimately plateau. This observation may have been affected as a result of the removal of metastatic tumors, already being advocated as one independent prognostic factor [11–15].

The present study had several limitations. This study was not prospective, and the study population may have a bias. Clinical follow-up after nephrectomy was usually performed using a CT scan, whereas FDG-PET was performed only in limited cases. Indeed, in the present study, patients whose prior CT scan suggested presence of recurrent tumors were the vast majority, and so the overall prevalence of recurrence in the study was as high as 75%. If clinical follow-up after nephrectomy had been performed using FDG-PET first, the prevalence of recurrence would not have been so high and the diagnostic accuracy might have been different. The prior CT scans were not standardized either as enhanced CT or as unenhanced CT. FDG-PET/CT is often reported superior to FDG-PET alone. In spite of these limitations, we believe that our study could favor the use of FDG-PET for postoperative surveillance in patients with RCC, and throughout almost 10 years of our institution's experience, we could undertake to determine whether FDG uptake could be a predictor of survival.

In conclusion, FDG-PET can be a complementary modality for postoperative surveillance in patients with RCC. Further investigations are needed to conclude whether PET can yield a prognostic value.

References

[1] Wahl RL, Harney J, Hutchins G, Grossman HB. Imaging of renal cancer using positron emission tomography with 2-deoxy-2-(18F)-fluoro-D-glucose: pilot animal and human studies. J Urol 1991;146(6):1470–4.
[2] Goldberg MA, Mayo-Smith WW, Papanicolaou N, Fischman AJ, Lee MJ. FDG PET characterization of renal masses: preliminary experience. Clin Radiol 1997;52(7):510–5.
[3] Montravers F, Grahek D, Kerrou K, et al. Evaluation of FDG uptake by renal malignancies (primary tumor or metastases) using a coincidence detection gamma camera. J Nucl Med 2000;41(1):78–84.
[4] Ramdave S, Thomas GW, Berlangieri SU, et al. Clinical role of F-18 fluorodeoxyglucose positron emission tomography for detection and management of renal cell carcinoma. J Urol 2001;166(3):825–30.
[5] Miyakita H, Tokunaga M, Onda H, et al. Significance of 18F-fluorodeoxyglucose positron emission tomography (FDG-PET) for detection of renal cell carcinoma and immunohistochemical glucose transporter 1 (GLUT-1) expression in the cancer. Int J Urol 2002;9(1):15–8.
[6] Aide N, Cappele O, Bottet P, et al. Efficiency of [(18)F]FDG PET in characterising renal cancer and detecting distant metastases: a comparison with CT. Eur J Nucl Med Mol Imaging 2003;30(9):1236–45.

Please cite this article in press as: Nakatani K, et al. The potential clinical value of FDG-PET for recurrent renal cell carcinoma. Eur J Radiol (2009), doi:10.1016/j.ejrad.2009.11.019

[7] Kang DE, White Jr RL, Zuger JH, Sasser HC, Teigland CM. Clinical use of fluorodeoxyglucose F 18 positron emission tomography for detection of renal cell carcinoma. J Urol 2004;171(5):1806–9.
[8] Safaei A, Figlin R, Hoh CK, et al. The usefulness of F-18 deoxyglucose whole-body positron emission tomography (PET) for re-staging of renal cell cancer. Clin Nephrol 2002;57(1):56–62.
[9] Majhail NS, Urbain JL, Albani JM, et al. F-18 fluorodeoxyglucose positron emission tomography in the evaluation of distant metastases from renal cell carcinoma. J Clin Oncol 2003;21(21):3995–4000.
[10] Jadvar H, Kherbache HM, Pinski JK, Conti PS. Diagnostic role of [F-18]-FDG positron emission tomography in restaging renal cell carcinoma. Clin Nephrol 2003;60(6):395–400.
[11] van der Poel HG, Roukema JA, Horenblas S, van Geel AN, Debruyne FM. Metastasectomy in renal cell carcinoma: a multicenter retrospective analysis. Eur Urol 1999;35(3):197–203.
[12] Antonelli A, Zani D, Cozzoli A, Cunico SC. Surgical treatment of metastases from renal cell carcinoma. Arch Ital Urol Androl 2005;77(2):125–8.
[13] Leibovich BC, Cheville JC, Lohse CM, et al. A scoring algorithm to predict survival for patients with metastatic clear cell renal cell carcinoma: a stratification tool for prospective clinical trials. J Urol 2005;174(5):1759–63.
[14] Eggener SE, Yossepowitch O, Kundu S, Motzer RJ, Russo P. Risk score and metastasectomy independently impact prognosis of patients with recurrent renal cell carcinoma. J Urol 2008;180(3):873–8.
[15] Crispen PL, Boorjian SA, Lohse CM, Leibovich BC, Kwon ED. Predicting disease progression after nephrectomy for localized renal cell carcinoma: the utility of prognostic models and molecular biomarkers. Cancer 2008;113(3):450–60.
[16] Montravers F, Rousseau C, Doublet JD, et al. In vivo inaccessibility of somatostatin receptors to 111In-pentreotide in primary renal cell carcinoma. Nucl Med Commun 1998;19(10):953–61.
[17] Gallagher BM, Fowler JS, Gutterson NI, MacGregor RR, Wan CN, Wolf AP. Metabolic trapping as a principle of radiopharmaceutical design: some factors responsible for the biodistribution of [18F] 2-deoxy-2-fluoro-D-glucose. J Nucl Med 1978;19(10):1154–61.
[18] Sengupta S, Lohse CM, Cheville JC, et al. The preoperative erythrocyte sedimentation rate is an independent prognostic factor in renal cell carcinoma. Cancer 2006;106(2):304–12.
[19] Lamb GW, McMillan DC, Ramsey S, Aitchison M. The relationship between the preoperative systemic inflammatory response and cancer-specific survival in patients undergoing potentially curative resection for renal clear cell cancer. Br J Cancer 2006;94(6):781–4.
[20] Araki K, Igarashi T, Tobe T, et al. Serum immunosuppressive acidic protein doubling time as a prognostic factor for recurrent renal cell carcinoma after nephrectomy. Urology 2006;68(6):1178–82.

Please cite this article in press as: Nakatani K, et al. The potential clinical value of FDG-PET for recurrent renal cell carcinoma. Eur J Radiol (2009), doi:10.1016/j.ejrad.2009.11.019

JOURNAL OF MAGNETIC RESONANCE IMAGING 30:678–683 (2009)

Technical Note

Visualization of External Carotid Artery and Its Branches: Non–contrast-Enhanced MR Angiography Using Balanced Steady-State Free-Precession Sequence and a Time-Spatial Labeling Inversion Pulse

Naoe Satogami, MD, Tomohisa Okada, MD, PhD,* Takashi Koyama, MD, PhD, Kimio Gotoh, MD, Toshikazu Kamae, MS, RT, and Kaori Togashi, MD, PhD

Purpose: To evaluate visibility of the external carotid artery (ECA) and its branches using three-dimensional (3D) balanced steady-state free-precession (SSFP) MR angiography with a time-spatial labeling inversion pulse (Time-SLIP), and to provide an optimal value of the inversion time (TI).

Materials and Methods: Peripheral-pulse-wave-gated 3D balanced SSFP images were obtained in 20 healthy volunteers. Images with a Time-SLIP using four different TIs (600, 900, 1200, and 1500 ms) and without a Time-SLIP, referred to as sequence A to E, were acquired for each subject and compared for visibility scores of ECA system and relative signal intensity (SI) of ECA.

Results: Average Friedman rank for overall visibility was 1.63, 3.01, 3.59, 3.58, and 3.20 for sequence A to E, respectively. Sequence C and D yielded significantly higher visibility than sequence A, B, and E. The mean relative SI value was 0.97, 0.87, 0.81, 0.76, and 0.67 for sequence A to E, respectively.

Conclusion: Balanced SSFP MR angiography with a Time-SLIP is superior to that without a Time-SLIP, showing excellent visualization of ECA system in approximately 3 min in average with sufficient background suppression including veins and salivary ducts. A TI of 1200 ms was considered to be optimal for this purpose.

Key Words: MR angiography; non–contrast-enhanced; external carotid artery; time-spatial labeling inversion pulse; balanced steady-state free-precession
J. Magn. Reson. Imaging 2009;30:678–683.

ANATOMICAL INFORMATION OF the external carotid artery (ECA) system has become more important for less-invasive treatment approaches to head and neck disorders (1–4), and time-of-flight (TOF) and phase-contrast (PC) imaging have been used for non–contrast-enhanced head and neck MR angiography (MRA) (5). However, saturation effects often lead to signal reduction of the ECA branches in TOF. In PC, motion artifacts caused by a long acquisition time can produce poor visualization of peripheral or movable branches, although the combined use of the parallel imaging and PC has shown good depiction of the ECA system (6).

Recently balanced steady-state free-precession (SSFP) sequence (also referred to as true fast imaging with steady-state precession [true FISP], fast imaging employing steady-state acquisition [FIESTA], balanced turbo field echo [bTFE], or true SSFP) has been applied to non–contrast-enhanced MRA of various regions including the coronary artery and hepatic vessels (7–9). Relatively good visualization of the ECA branches with balanced SSFP has been reported in face and neck region (6,10). However, veins and salivary gland ducts also show high signal intensity in this sequence, which becomes problematic for vessel identification, especially in maximum intensity projection (MIP) images.

To overcome this problem, the time-spatial labeling inversion pulse (Time-SLIP) method can be adopted, although there have been no reports in the literature regarding visibility of the ECA branches with use of Time-SLIP, to the best of our knowledge. It applies a selective inversion pulse before data acquisition and suppresses the background signal, thus provides selective blood inflow information (7). The alteration of the inversion time (TI) in Time-SLIP can control the extent of inflowing arterial signal and background signal suppression. The purpose of this study was to evaluate visibility of the ECA and its branches using balanced SSFP imaging with a Time-SLIP, and provide an optimal TI value for this protocol.

MATERIALS AND METHODS

Subjects

Twenty healthy volunteers (14 men and 6 women; mean age, 24 years; age range, 18–31 years) were included in this study, which was approved by the local ethics com-

Department of Diagnostic Imaging and Nuclear Medicine, Kyoto University Graduate School of Medicine, Kyoto, Japan.
Contract grant sponsor: R&D of Molecular Imaging Equipment for Malignant Tumor Therapy Support, supported by NEDO (New Energy and Industrial Technology Development Organization), Japan.
*Address reprint requests to: T.O., Department of Diagnostic Imaging and Nuclear Medicine, Kyoto University Graduate School of Medicine, 54 Kawahara-cho, Shogoin, Sakyo-ku, Kyoto 606-8507, Japan. E-mail: tomokada@kuhp.kyoto-u.ac.jp
Received March 7, 2009; Accepted June 12, 2009.
DOI 10.1002/jmri.21883
Published online in Wiley InterScience (www.interscience.wiley.com).

mittee. All subjects provided written informed consent before the examination.

MR Imaging

All MR examinations were conducted using a 1.5 Tesla (T) MR scanner (EXCELART Vantage, powered by Atlas; Toshiba Medical Systems, Tokyo, Japan) with a head and neck coil and the uppermost row of a spine coil. Before MRA acquisition, a peripheral-pulse-wave-gated preparation scan was performed to select a proper delay time from a pulse-wave trigger. Several coronal SSFP images at different times from the trigger were acquired with the following parameters: repetition time (TR), 4.2 ms; echo time (TE), 2.1 ms; flip angle, 63 degree; field of view (FOV), 225 × 300 mm; matrix, 192 × 256; slice thickness, 10 mm; slice number, 3; acquisition time, 51 s in average. An appropriate delay time was visually selected for each subject to avoid signal void by arterial flow.

For MRA, peripheral-pulse-wave-gated three-dimensional (3D) balanced SSFP images with fat saturation were obtained in coronal plane. Imaging parameters were as follows: TR, 4.3 ms; TE, 2.2 ms; flip angle, 120 degree; FOV, 180 × 320 mm; matrix, 144 × 256; slice thickness, 1.5 mm; slice number, 54; number of acquisition, 1; parallel imaging factor, 2 in the phase encoding direction. The raw data was zero-filled and final apparent resolution was 0.6 × 0.6 × 0.75 mm. The posterior border of the FOV was located approximately at the posterior edge of the vertebral body of the upper cervical spine (Fig. 1). For each subject, five balanced SSFP sequences were performed: balanced SSFP with a Time-SLIP using four different TIs (600, 900, 1200, and 1500 ms) and balanced SSFP without a Time-SLIP. The acquisition time for each sequence ranged from 1 min 50 s to 4 min 15 s (mean, 3 min 13 s) according to pulse rates of the subjects.

In balanced SSFP sequences with a Time-SLIP, a spatially selective inversion-recovery pulse with 230-mm width was placed above the inferior edge of the mandible (Fig. 1). After each TI, inflowing arterial signal was depicted as bright-blood with variable background signal suppression above the distal common carotid artery, covering the ECA system.

Image Analysis

The five MRA sequences were referred to as sequence A (TI of 600 ms), sequence B (TI of 900 ms), sequence C (TI of 1200 ms), sequence D (TI of 1500 ms), and sequence E (without a Time-SLIP). MIP images were reconstructed from the coronal source images of each sequence into 40 projections rotating around the craniocaudal axis at 9-degree increments. All qualitative and quantitative imaging evaluations were performed using OsiriX Medical Imaging Software (http://www.osirix-viewer.com/).

Qualitative Evaluation

The acquired images were assessed in two ways: "MIP" evaluation (with MIP images only) and "source" evaluation (with both MIP images and coronal source images).

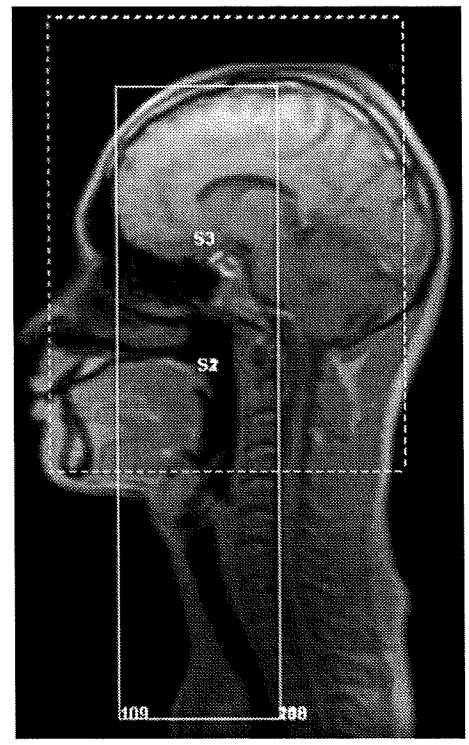

Figure 1. A representative scout image with scan planning. The posterior border of the imaged area (continuous line) is located approximately at the posterior edge of the vertebral body of the upper cervical spine. The inferior border of the inversion pulse (dotted line) is placed near the inferior edge of the mandible.

In "MIP" evaluation, a total of nine segments of the ECA system: the main ECA and eight first-order branches (the superior thyroid, lingual, facial, ascending pharyngeal, occipital, posterior auricular, maxillary, and superficial temporal artery), were evaluated for sequences A, B, C, and D. Sequence E (without a Time-SLIP) was not evaluated because separation of arteries from veins and salivary gland ducts was difficult with MIP images only. In "source" evaluation, a total of 11 segments of the ECA system: the main ECA, 8 first-order branches, and 2 second-order branches (the middle meningeal and deep lingual artery), were evaluated for sequences A, B, C, D, and E. These two second-order branches were selected for the evaluation because they showed relatively good visibility in a previous study (6), and were completely covered in the FOV in our study.

For both evaluations, two radiologists (N.S. with 7 years of experience and K.G. with 6 years of experience) independently scored visibility of each ECA segment. Visualization quality was scored on a 4-point scale: 1, not visible; 2, poor image quality, visibility of only the origin of the segment; 3, moderate image quality, visibility of the proximal portion of the segment; and 4, good image quality, visibility of the complete course of the segment. The right and left sides were separately scored. The complete course of several ECA branches, especially the occipital and posterior auricular artery, was not covered in some subjects because of FOV constraints, and these segments were scored as 4 for de-

Table 1
Mean Visibility Scores of the External Carotid Segments in "MIP" Evaluation*

	Sequence A (TI of 600 ms)	Sequence B (TI of 900 ms)	Sequence C (TI of 1200 ms)	Sequence D (TI of 1500 ms)
External carotid	3.8 ± 0.3	4.0 ± 0.0	4.0 ± 0.0	4.0 ± 0.0
Superior thyroid	2.2 ± 0.7	3.1 ± 0.6	3.4 ± 0.7	3.3 ± 0.9
Lingual	2.3 ± 0.5	3.4 ± 0.6	3.9 ± 0.3	3.9 ± 0.2
Facial	2.7 ± 0.8	3.6 ± 0.6	3.9 ± 0.4	3.9 ± 0.4
Ascending pharyngeal	1.1 ± 0.2	1.4 ± 0.7	1.7 ± 1.0	1.5 ± 0.9
Occipital	3.7 ± 0.8	3.9 ± 0.3	4.0 ± 0.1	3.9 ± 0.5
Posterior auricular	1.3 ± 0.8	2.7 ± 1.3	3.0 ± 1.2	2.6 ± 1.4
Maxillary	2.2 ± 0.6	3.3 ± 0.7	3.9 ± 0.3	3.9 ± 0.2
Superficial temporal	2.2 ± 0.7	3.5 ± 0.7	3.9 ± 0.2	4.0 ± 0.1
Average Friedman rank	1.51	2.53	3.02[a]	2.94[a]

*No significant difference is observed between sequences C and D ($P = 0.201$).
[a]$P < 0.001$ by pair-wise comparisons with sequences A and B.

scriptive purposes when they were entirely visualized in the applied FOV. "MIP" and "source" evaluations were performed separately with random orders. In "MIP" evaluation each observer scored 18 segments for each sequence in 20 subjects, constituting a total of 1440 segments. In "source" evaluation each observer scored 22 segments for each sequence in 20 subjects, constituting a total of 2200 segments.

Quantitative Evaluation

Relative signal intensity (SI) of the target organ compared with that of reference tissue was adopted for quantitative evaluation (11), because the conventionally used method to determine the signal-to-noise ratio (SNR), which is derived from two separate regions of interest (ROIs) in a single image, was difficult to apply due to the use of the parallel imaging (12). The SI of the ECA was compared with that of the muscle adjacent to it for all sequences. The average SI of the main ECA and the sternocleidomastoid muscle were measured by applying oval ROIs on the coronal source images. An ROI was manually placed at the origin of the main ECA on the right side. If the lumen of the artery showed marked heterogeneous intensity due to flow related effect, an ROI was placed at the origin of the contralateral (left) ECA. Another ROI was placed at the belly of the sternocleidomastoid muscle with homogenous signal intensity on the same side as the ROI of the artery. In each subject, ROIs of the artery were of the same shape and area for all MRA sequences and were placed on the same side and position of the main ECA; ditto with ROIs of the muscle. The range of the area of ROIs was 15–17 mm^2 for the ECA and 30–33 mm^2 for the sternocleidomastoid muscle, respectively. The relative SI, that is, the artery–muscle contrast was calculated by the following equation: relative SI = $(SI_{artery} - SI_{muscle}) / SI_{artery}$.

Statistical Analysis

All statistical analyses were conducted using SPSS software, version 12.0 (SPSS, Inc., Chicago, IL). For qualitative assessment, the degree of interobserver agreement was calculated using the Cohen's kappa test (a value of 0.21–0.40, fair agreement; 0.41–0.60, moderate agreement; 0.61–0.80, substantial agreement; 0.81–1.00, excellent agreement). Based on this result, all statistical analyses were performed using an average score of two readers for each segment. Friedman's nonparametric test was used to evaluate intersequence differences in visibility of the ECA system. A P value of less than 0.05 was considered to indicate a statistically significant difference. Wilcoxon signed-rank test with Bonferroni correction was applied for multiple pair-wise comparisons. A P value of less than 0.009 and 0.005 was considered to indicate a statistically significant difference in "MIP" evaluation and "source" evaluation, respectively.

For quantitative assessment, one-way repeated-measures analysis of variance (ANOVA) was performed for the assessment of intersequence differences in the relative SI. Scheffe's test was applied as post hoc testing for multiple comparisons. A P value of less than 0.05 was considered to indicate a statistically significant difference.

RESULTS

Qualitative Analysis

The Cohen's kappa test showed nearly almost perfect interreader agreement for "MIP" evaluation (kappa = 0.80) as well as "source" evaluation (kappa = 0.79). The scores for visibility of the ECA segments and average Friedman rank of each sequence for "MIP" and "source" evaluations were summarized in Tables 1 and 2, respectively. The Friedman's nonparametric test showed significant differences both in "MIP" and "source" evaluations ($P < 0.001$). In "MIP" evaluation, sequence A revealed the lowest values compared with the other sequences ($P < 0.001$). The scores of sequence B also showed significant deterioration in comparison with sequences C and D ($P < 0.001$). No significant difference was observed between sequence C and D ($P = 0.201$), although sequence C had slightly higher average Friedman rank (Figs. 2, 3). In "source" evaluation, visibility was significantly deteriorated in sequence A in comparison with the others ($P < 0.001$). The scores between sequence B and E revealed no significant difference ($P = 0.108$), but both sequence B and E yielded lower values compared with sequence C and D ($P < 0.001$). The scores of sequences C and D did not differ ($P = 0.961$).

Table 2
Mean Visibility Scores of the External Carotid Segments in "Source" Evaluation*

	Sequence A (TI of 600 ms)	Sequence B (TI of 900 ms)	Sequence C (TI of 1200 ms)	Sequence D (TI of 1500 ms)	Sequence E (without a Time-SLIP)
External carotid	3.9 ± 0.2	4.0 ± 0.0	4.0 ± 0.0	4.0 ± 0.0	4.0 ± 0.0
Superior thyroid	2.6 ± 0.6	3.3 ± 0.6	3.6 ± 0.6	3.7 ± 0.6	3.4 ± 0.9
Lingual	2.6 ± 0.5	3.7 ± 0.4	4.0 ± 0.2	4.0 ± 0.1	4.0 ± 0.0
Facial	3.1 ± 0.7	3.8 ± 0.5	3.9 ± 0.3	4.0 ± 0.3	3.9 ± 0.3
Ascending pharyngeal	1.6 ± 0.6	2.5 ± 0.9	2.9 ± 1.0	2.6 ± 1.1	2.0 ± 1.1
Occipital	4.0 ± 0.1	4.0 ± 0.0	4.0 ± 0.0	4.0 ± 0.0	4.0 ± 0.1
Posterior auricular	2.3 ± 1.1	3.4 ± 0.9	3.7 ± 0.7	3.6 ± 0.9	3.1 ± 1.2
Maxillary	2.6 ± 0.6	3.6 ± 0.5	3.9 ± 0.3	4.0 ± 0.1	3.8 ± 0.5
Superficial temporal	2.9 ± 0.6	3.8 ± 0.5	4.0 ± 0.0	4.0 ± 0.0	4.0 ± 0.1
Middle meningeal	1.8 ± 0.7	3.3 ± 0.8	3.8 ± 0.5	3.6 ± 0.6	2.5 ± 0.9
Deep lingual	1.1 ± 0.3	2.5 ± 1.1	3.7 ± 0.6	3.9 ± 0.3	4.0 ± 0.2
Average Friedman rank	1.63	3.01[a]	3.59[a,b]	3.58[a,b]	3.20[a]

*No significant difference is observed between sequences C and D ($P = 0.961$).
[a]$P < 0.001$ by pair-wise comparisons with sequence A.
[b]$P < 0.001$ by pair-wise comparisons with sequence B or E.

Quantitative Analysis

The relative SI values were 0.97 ± 0.02, 0.87 ± 0.02, 0.81 ± 0.02, 0.76 ± 0.02, and 0.67 ± 0.03 (mean ± standard deviation) for sequence A, B, C, D, and E, respectively. The relative SI values were largest with sequence A, second largest with sequence B, third largest with sequence C, fourth largest with sequence D, and lowest with sequence E ($P < 0.001$ for all pair-wise comparisons).

DISCUSSION

Several less-invasive treatment approaches using catheter-directed selective angiographic techniques have been more and more applied to head and neck diseases, including selective arterial embolization (1), preoperative endovascular embolization (2,3), and selective intra-arterial infusion chemotherapy (4). Detailed preoperative anatomical information of the ECA system is especially important for these treatment approaches.

Contrast-enhanced MRA has been applied to the ECA system and high-resolution images can be obtained especially on 3T MRI units (13), although it has some disadvantages such as potential nephrotoxicity and association with nephrogenic systemic fibrosis (14). Computed tomography angiography can also be used for the external carotid evaluation (15), but radiation exposure is inevitable and iodine-based contrast materials are potentially nephrotoxic (16) and have a relatively high risk of allergic adverse reactions (17).

Recently Sumi et al (6) applied balanced SSFP sequence to MRA of the ECA system. Balanced SSFP is a special type of rapid gradient-echo sequence in which the imaging gradients are fully balanced without an influence on the transverse magnetization (18). This sequence provides a rapid imaging with a very high SNR, and the intrinsic image contrast is determined by T2/T1 ratio of the tissue. A strong contrast between the blood vessels and muscle can be obtained, but veins and salivary gland ducts as well as arteries show high signal intensity. Sumi et al (6) stated that an effective method of separating arteries from veins and salivary gland ducts was needed for balanced SSFP MRA.

The time-SLIP technique is a useful method to depict arteries selectively with good background signal suppression without use of contrast materials (19), and it can be applied to balanced SSFP. A spatially selective inversion-recovery pulse is placed before data acquisition, and blood inflowing into the desired imaging area during an inversion time is depicted as bright while suppressed background signal is gradually recovering. Better background suppression and less peripheral branch depiction are observed with a shorter TI, while a longer TI enables better visualization of peripheral branches although background signal recovery may mask inflowing blood signal. Concerning an optimal TI value of the current study, sequence C (TI of 1200 ms) and D (TI of 1500 ms) showed higher visibility compared with sequence A and B in both "MIP" and "source" evaluations. Better background suppression, that is, a higher relative SI value was observed in sequence C compared with sequence D, and a TI of 1200 ms was suggested to be an optimal value in our protocol.

Theoretically, balanced SSFP with a Time-SLIP cannot visualize the entire ECA system to the same level as that without a Time-SLIP on the source images, because a spatially selective inversion-recovery pulse suppresses arterial signal in the imaged area to some extent. However, our results showed that balanced SSFP with a time-SLIP with a relatively long TI (sequence C and D) showed higher visibility than sequence E even in "source" evaluation. Better background suppression including veins and salivary gland ducts may help more confident identification and tracking of the ECA segments.

There are several limitations in our study. First, conventional angiography was not performed in any subjects, which would have been a reference standard for the anatomical evaluation. However, most ECA branches could be identified with confidence in our study, and our main purpose was the optimization of the imaging protocols. Second, balanced SSFP MRA with a Time-SLIP was not compared with PC MRA. Sumi

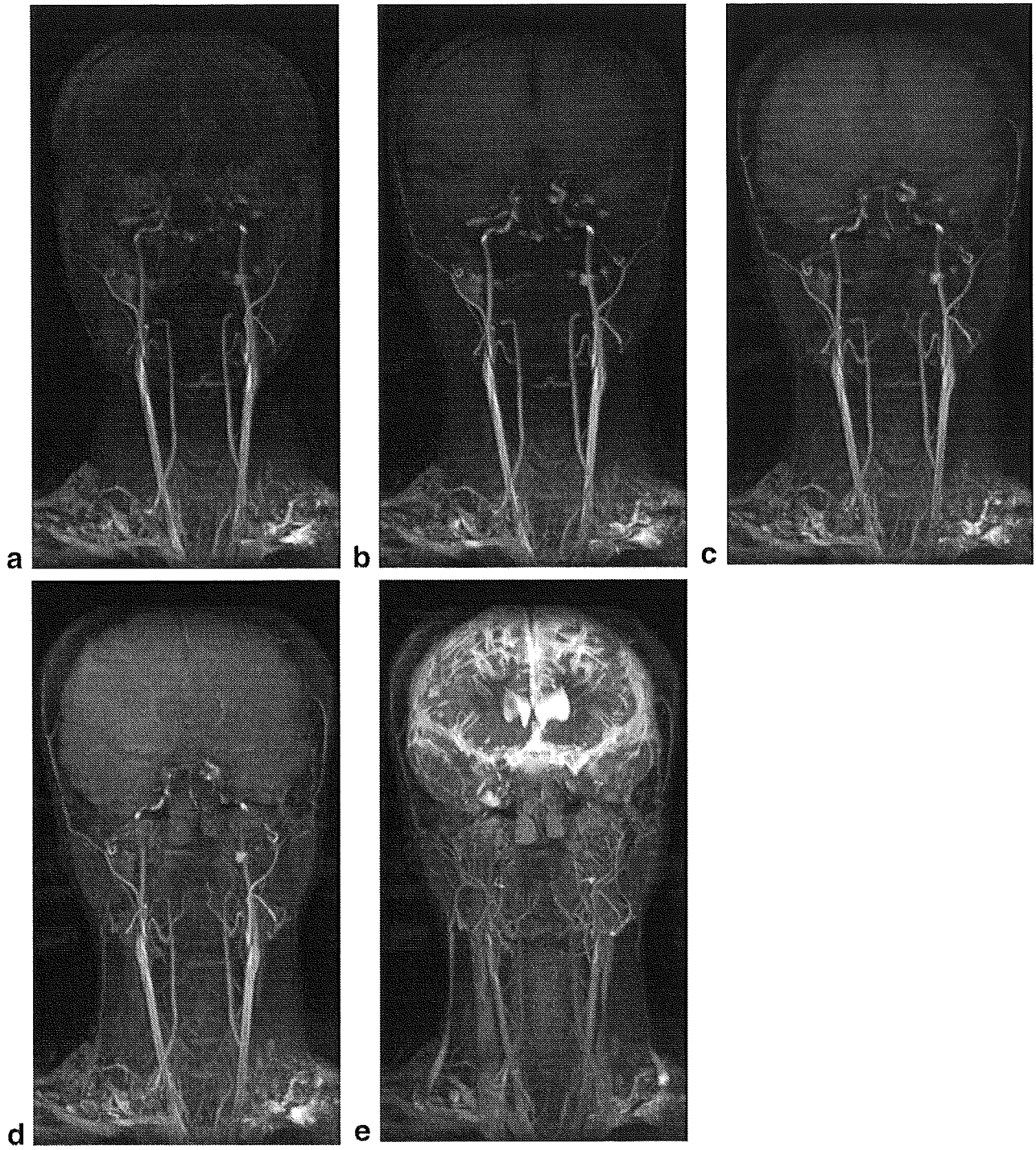

Figure 2. Visualization of the external carotid artery system with different TIs (coronal MIP images of a 25-year-old man). **a–e:** Sequences A–D with a Time-SLIP using a TI of 600 (a), 900 (b), 1200 (c), and 1500 (d) ms, and sequence E (e, without a Time-SLIP). Background signal was better suppressed for shorter TIs (see a,b), but more peripheral branches were visualized with the increase of TI (see c,d). Note complicated signals without a Time-SLIP (e).

et al (6) reported that PC with the parallel imaging performed the best for overall visibility of the ECA system among TOF, PC, and balanced SSFP, although arterial spin-labeling method was not used in their study. We did not assess PC MRA because the parallel imaging was not available for PC sequence in the MR scanner used in this study. Another limitation is that a time-resolved display of the neovascularization of tumors that is enabled by using contrast-enhancement (20) is not capable in the current method.

In conclusion, this is the first report evaluating visibility of the external carotid artery and its branches in balanced SSFP sequence with the Time-SLIP method, to the best of our knowledge. Balanced SSFP MRA with a Time-SLIP allows excellent visualization of the external carotid artery system in around 3 min with sufficient

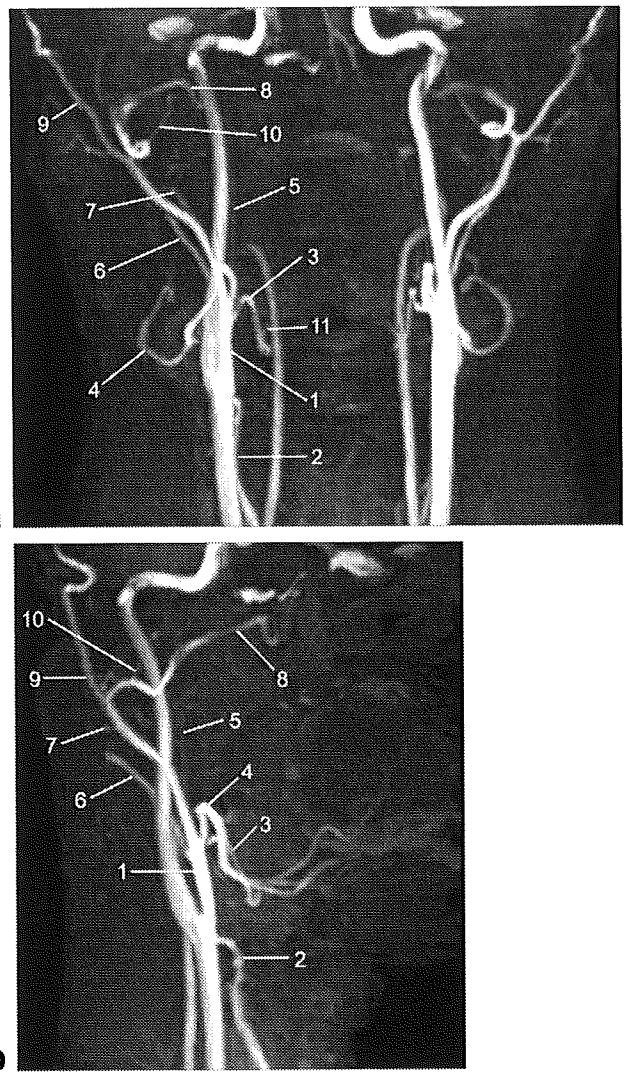

Figure 3. Balanced SSFP MR angiography of the external carotid artery system with a Time-SLIP using the optimal TI of 1200 ms in a 23-year-old man. **a,b:** Coronal (a) and oblique-lateral (b) MIP images. Good visualization was obtained for the external carotid artery and its branches: (1) the main external carotid artery, (2) superior thyroid artery, (3) lingual artery, (4) facial artery, (5) ascending pharyngeal artery, (6) occipital artery, (7) posterior auricular artery, (8) maxillary artery, (9) superficial temporal artery, (10) middle meningeal artery, and (11) deep lingual artery.

background signal suppression inclusive of veins and salivary gland ducts. A TI of 1200 ms was considered to be optimal for this purpose.

REFERENCES

1. Elden L, Montanera W, Terbrugge K, Willinsky R, Lasjaunias P, Charles D. Angiographic embolization for the treatment of epistaxis: a review of 108 cases. Otolaryngol Head Neck Surg 1994; 111:44–50.
2. Marshall AH, Bradley PJ. Management dilemmas in the treatment and follow-up of advanced juvenile nasopharyngeal angiofibroma. ORL J Otorhinolaryngol Relat Spec 2006;68:273–278.
3. Kasper GC, Welling RE, Wladis AR, et al. A multidisciplinary approach to carotid paragangliomas. Vasc Endovascular Surg 2006; 40:467–474.
4. Tsurumaru D, Kuroiwa T, Yabuuchi H, Hirata H, Higaki Y, Tomita K. Efficacy of intra-arterial infusion chemotherapy for head and neck cancers using coaxial catheter technique: initial experience. Cardiovasc Intervent Radiol 2007;30:207–211.
5. van den Berg R, Wasser MN, van Gils AP, van der Mey AG, Hermans J, van Buchem MA. Vascularization of head and neck paragangliomas: comparison of three MR angiographic techniques with digital subtraction angiography. AJNR Am J Neuroradiol 2000;21:162–170.
6. Sumi T, Sumi M, Van Cauteren M, Kimura Y, Nakamura T. Parallel imaging technique for the external carotid artery and its branches: comparison of balanced turbo field echo, phase contrast, and time-of-flight sequences. J Magn Reson Imaging 2007;25:1028–1034.
7. Miyazaki M, Lee VS. Nonenhanced MR angiography. Radiology 2008;248:20–43.
8. Okada T, Kanao S, Ninomiya A, et al. Whole-heart coronary magnetic resonance angiography with parallel imaging: comparison of acceleration in one-dimension vs. two-dimensions. Eur J Radiol 2008;Jul 19. DOI: 10.1016/j.ejrad.2008.06.005.
9. Shimada K, Isoda H, Okada T, et al. Non-contrast-enhanced MR angiography for selective visualization of the hepatic vein and inferior vena cava with true steady-state free-precession sequence and time-spatial labeling inversion pulses: preliminary results. J Magn Reson Imaging 2009;29:474–479.
10. Koktzoglou I, Edelman RR. Fast projective carotid MR angiography using arterial spin-labeled balanced SSFP. J Magn Reson Imaging 2008;28:778–782.
11. Xu PJ, Yan FH, Wang JH, Lin J, Fan J. Utilizing generalized autocalibrating partial parallel acquisition (GRAPPA) to achieve high-resolution contrast-enhanced MR angiography of hepatic artery: initial experience in orthotopic liver transplantation candidates. Eur J Radiol 2007;61:507–512.
12. Dietrich O, Raya JG, Reeder SB, Reiser MF, Schoenberg SO. Measurement of signal-to-noise ratios in MR images: influence of multichannel coils, parallel imaging, and reconstruction filters. J Magn Reson Imaging 2007;26:375–385.
13. Lohan DG, Barkhordarian F, Saleh R, et al. MR angiography at 3 T for assessment of the external carotid artery system. AJR Am J Roentgenol 2007;189:1088–1094.
14. Marckmann P, Skov L, Rossen K, et al. Nephrogenic systemic fibrosis: suspected causative role of gadodiamide used for contrast-enhanced magnetic resonance imaging. J Am Soc Nephrol 2006; 17:2359–2362.
15. Lell M, Tomandl BF, Anders K, Baum U, Nkenke E. Computed tomography angiography versus digital subtraction angiography in vascular mapping for planning of microsurgical reconstruction of the mandible. Eur Radiol 2005;15:1514–1520.
16. Morcos SK, Thomsen HS, Webb JA. Contrast-media-induced nephrotoxicity: a consensus report. Contrast Media Safety Committee, European Society of Urogenital Radiology (ESUR). Eur Radiol 1999; 9:1602–1613.
17. Namasivayam S, Kalra MK, Torres WE, Small WC. Adverse reactions to intravenous iodinated contrast media: a primer for radiologists. Emerg Radiol 2006;12:210–215.
18. Scheffler K, Lehnhardt S. Principles and applications of balanced SSFP techniques. Eur Radiol 2003;13:2409–2418.
19. Garcia DM, Duhamel G, Alsop DC. Efficiency of inversion pulses for background suppressed arterial spin labeling. Magn Reson Med 2005;54:366–372.
20. Michaely HJ, Herrmann KA, Dietrich O, Reiser MF, Schoenberg SO. Quantitative and qualitative characterization of vascularization and hemodynamics in head and neck tumors with a 3D magnetic resonance time-resolved echo-shared angiographic technique (TREAT)—initial results. Eur Radiol 2007;17:1101–1110.

AJR FOCUS ON:

Unenhanced MR Portography With a Half-Fourier Fast Spin-Echo Sequence and Time–Space Labeling Inversion Pulses: Preliminary Results

Kotaro Shimada[1]
Hiroyoshi Isoda
Tomohisa Okada
Toshikazu Kamae
Shigeki Arizono
Yuusuke Hirokawa
Kaori Togashi

OBJECTIVE. For this study, we aimed to selectively visualize the intrahepatic portal veins using 3D half-Fourier fast spin-echo (FSE) MR angiography (MRA) with a time–space labeling inversion pulse (T-SLIP) and to optimize the acquisition protocol.

SUBJECTS AND METHODS. Respiratory-triggered 3D half-Fourier FSE scans were obtained in 25 healthy adult subjects combined with two different T-SLIPs: one placed on the liver and the thorax to suppress signals of the liver parenchyma, hepatic veins, and abdominal arteries and the other on the lower abdomen to suppress the ascending signal of the inferior vena cava. One of the most important factors was the inversion time (TI) of the inversion pulse for the liver and thorax. Image quality was evaluated in terms of signal-to-noise ratio, contrast-to-noise ratio, and mean visualization scores at four different TIs: 800, 1,200, 1,600, and 2,000 milliseconds.

RESULTS. Selective visualization of the portal vein was successfully achieved in all volunteers, and anatomic variations were also seen in three subjects. A TI of 1,200 milliseconds was optimal in our protocol because it was sufficient for peripheral portal vein visualization and was most suitable for signal suppression of the hepatic veins and liver parenchyma.

CONCLUSION. Half-Fourier FSE scanning with T-SLIPs enabled selective visualization of the portal vein without an exogenous contrast agent.

Precise delineation of the portal venous anatomy is essential when assessing patients before hepatectomy or liver transplantation [1]. Contrast-enhanced angiography with CT or MRI is a standard and noninvasive procedure for this purpose [2, 3]. However, both CT and MR contrast agents have side effects, such as anaphylactic shock. In addition, they should not be administered to patients with decreased renal function [4].

Recently, unenhanced MR angiography (MRA) techniques, such as 3D half-Fourier fast spin-echo (FSE) and true steady-state free precession (SSFP), have allowed rapid progress and are being effectively used for visualization of the coronary arteries, renal arteries, and peripheral vessels [5–7]. Unenhanced visualization of the hepatic artery has recently been reported [8]; however, for the portal vein, analysis of only intraportal blood flow distribution has been reported [9]. Those investigators used a half-Fourier FSE technique to make the most of the T2 blurring effect [10] and near-the-center-of-k-space acquisition. The 3D half-Fourier FSE method is one of the new MRA techniques that allows selective visualization of fluid components (i.e., blood) in arteries and veins. In general, an FSE sequence uses a long TE value and shows rapid blood flow as signal void; however, reduced echo-train spacing enables compact echo sampling and reduces this phenomenon, especially when the flow velocity is low, as in the vein [6]. This technique can show slow blood flow, such as portal venous flow, as high signal intensity without the use of a gadolinium-based contrast agent. However, with this technique alone, it is difficult to visualize the portal vein selectively because of overlaps of the hepatic arterial and venous systems.

The time–space labeling inversion pulse (T-SLIP) method is a form of spin labeling that can provide quantitative and selective inflow information by placing the inversion pulse before data acquisition and suppressing the background [11]. A T-SLIP can also be used for selective suppression of the blood signal when it is placed on a vessel of no interest. More than one T-SLIP can be placed arbitrarily independent of the imaging area,

Keywords: liver, MR angiography, MR portography, MR pulses, MR technique, portal vein, T-SLIP

DOI:10.2214/AJR.08.1626

Received August 2, 2008; accepted after revision January 1, 2009.

This study was conducted as a part of the project "R&D of Molecular Imaging Equipment for Malignant Tumor Therapy Support" and was supported by the New Energy and Industrial Technology Development Organization, Japan.

[1]All authors: Department of Diagnostic Imaging and Nuclear Medicine, Kyoto University Graduate School of Medicine, 54 Kawahara-cho, Shogoin, Sakyo-ku, Kyoto 606-8507, Japan. Address correspondence to K. Shimada (kotaro@kuhp.kyoto-u.ac.jp).

AJR 2009; 193:106–112

0361–803X/09/1931–106

and the T-SLIP method enables selective visualization of the vessel of interest. By changing the inversion time (TI), the T-SLIP method can control the extent of the inflowing blood signal.

To date, the use of unenhanced MRA for selective visualization of the intrahepatic portal system has not been fully evaluated. The purpose of our study was to selectively visualize the portal vein using respiratory-triggered 3D half-Fourier FSE imaging with T-SLIPs and to determine the optimal protocol for its visualization. Herein, we report our initial experience.

Subjects and Methods

Subjects

This study was conducted in accordance with the ethical standards of the World Medical Association (Declaration of Helsinki). From April 2008 to June 2008, 25 healthy adult subjects (18 men and seven women; average age, 28 years; age range, 18–44 years) were included in this study. Institutional review board approval and written informed consent from all subjects were obtained before MRI examinations. All subjects were instructed to breathe normally during scanning.

MRI Protocol

Each examination was conducted with the subject in the supine position using a 1.5-T MRI system (EXCELART Vantage powered by Atlas, Toshiba Medical Systems) equipped with a pair of 4 × 4 phased-array coils placed at both the front and back of the abdomen. Two rows were used for both the front and back coils, resulting in 16 active coil elements connected to 16 receiver channels.

To localize the heart and liver for placement of two different T-SLIPs, coronal true SSFP images without an inversion pulse were acquired using the following parameters: TR/TE, 5.2/2.6; flip angle, 65°; field of view, 400 × 400 mm; matrix, 256 × 256; number of slices, 16; and slice thickness, 10 mm. To visualize the intrahepatic portal venous system selectively, respiratory-triggered 3D single-shot half-Fourier FSE images with fat saturation were acquired in the coronal plane using two T-SLIPs (a work-in-progress sequence from the vendor) at different locations and with a different TI as described in the next section.

Respiratory triggering was conducted at the beginning of expiration using a bellows wrapped around the patient's abdomen to reduce motion artifacts. The scanning parameters were as follows: 1 respiration interval/80; flip angle, 90°; echo-train spacing, 5 milliseconds; slice thickness, 3 mm; number of slices, 35 and no gap; field of view, 370 × 400 mm; receiver bandwidth, 651 Hz/pixel; matrix size, 256 × 256; number of acquisitions, 1; and parallel imaging factor of 2 in the phase direction, resulting in the collection of 128 phase-encoding lines per respiratory trigger in a centric order.

The final images were reconstructed into apparent spatial resolutions of 0.7 × 0.8 × 1.5 mm. The acquisition time of each scan ranged from 3 to 4 minutes. The reduction in the echo-train spacing reduces the single-shot acquisition time, which effectively reduces motion-related artifacts and minimizes susceptibility effects, resulting in constant depiction of the peripheral vein throughout the cardiac cycle [6]. In addition, central k-space ordering reduces flow voids in the phase-encode direction. For these reasons, neither cardiac triggering nor a subtraction method was used.

Application of T-SLIPs

Two different oblique T-SLIPs were used (Fig. 1): One was placed on the liver and the thorax to cover the liver, heart, and thoracic descending aorta and suppress signal of the liver parenchyma, hepatic vein, and abdominal aorta. Its thickness was 150 mm. Four different TIs—800, 1,200, 1,600, and 2,000 milliseconds—were used to investigate the optimal TI for selective visualization of the portal venous system.

The other T-SLIP was placed on the lower abdomen caudad to the line between the inferior edge of the liver and the bifurcation of the abdominal aorta. The plane of this T-SLIP was oblique to minimize saturation of inflow signals to the liver from mesenteric veins and to suppress the ascending signal of the inferior vena cava (IVC) to the liver and avoid overlap of IVC signal with that of the portal vein. The thickness of this T-SLIP was 200 mm. The TI of this pulse was fixed to 1,100 milliseconds because it was near the null point of the venous blood [12] and gave enough time for the suppressed blood to flow into the upper abdominal region. The total scanning times were approximately 20 minutes, including scans at four different TIs for all volunteers.

Data Analysis

According to the difference in TIs of the T-SLIP placed on the liver and the thorax, four scanning parameter groups were created: group A, TIs of 800 and 1,100 milliseconds; group B, TIs of 1,200 and 1,100 milliseconds; group C, TIs of 1,600 and 1,100 milliseconds; and group D, TIs of 2,000 and 1,100 milliseconds. The acquired images were compared to detect the optimal TI for selective visualization of the portal venous system using maximum-intensity-projection (MIP) images and source images. All quantitative and qualitative assessments of image quality were performed on a commercially available workstation (Ziostation, Ziosoft).

Region-of-Interest (ROI) Analysis

On the coronal source images, ROIs were placed manually in the right portal vein (RPV) and left portal vein (LPV) and drawn as large as possible (mean, 48 mm^2; range, 26–77 mm^2). An ROI in the RPV was placed near the bifurcation of anterior and posterior segment branches, and an ROI in the LPV was placed in the umbilical portion. An ROI in the liver parenchyma was at least 40 mm^2 and was located in a homogeneous portion of the liver devoid of vessels and prominent artifacts and close to the portal vein. ROIs were drawn three times at each position, and the mean signal intensity (SI) values were adopted. Because the SD of the background noise could not be used to calculate the image signal-to-noise ratio (SNR) due to the use of the parallel imaging technique, we calculated SD of signal values in the ROI at the liver parenchyma as the noise (SD_{noise}) [13]. The SNR and contrast-to-noise ratio (CNR) were calculated using the following formulas:

$$SNR_{vessel} = SI_{vessel} / SD_{noise}$$

and

$$CNR_{vessel\text{-}liver} = (SI_{vessel} - SI_{liver}) / SD_{noise}.$$

SI_{liver} and SI_{vessel} are the mean signal intensity of ROIs in liver parenchyma and vessels—that is, the RPV and LPV, respectively. $CNR_{vessel\text{-}liver}$ is contrast-to-noise ratio of the vessels compared with the liver parenchyma.

Qualitative Analysis

The images were scored in consensus by two experienced radiologists (18 and 8 years of experience) who were blinded to the scanning conditions for visualization of the main trunk of the RPV and LPV and the portal branches of segments IV and VIII (P4 and P8, respectively). The visualization scores were evaluated using a 4-point scale: 1, not visible or nondiagnostic image quality; 2, poor image quality without sufficient visualization; 3, good image quality sufficient for diagnosis; or 4, excellent image quality with sharply defined vessels. Additional evaluation was conducted as to the overall image quality on arterial or venous overlap and motion artifact with a 3-point scale: 1, severe; 2, moderate; or 3, minimal [6].

Statistical Analysis

Statistical analyses were performed using a commercially available software package (Statview, version 5.0.1, SAS Institute). Comparisons of SNR and CNR were conducted using one-way repeated-measures analysis of variance followed by a post-hoc test. For the qualitative results of the different protocol groups, visualization scores and scores for overall image quality were compared using Friedman's nonparametric test and Scheffe's test.